Article

Cell

Functional Selectivity in Cytokine Signaling Revealed Through a Pathogenic *EPO* Mutation

Graphical Abstract

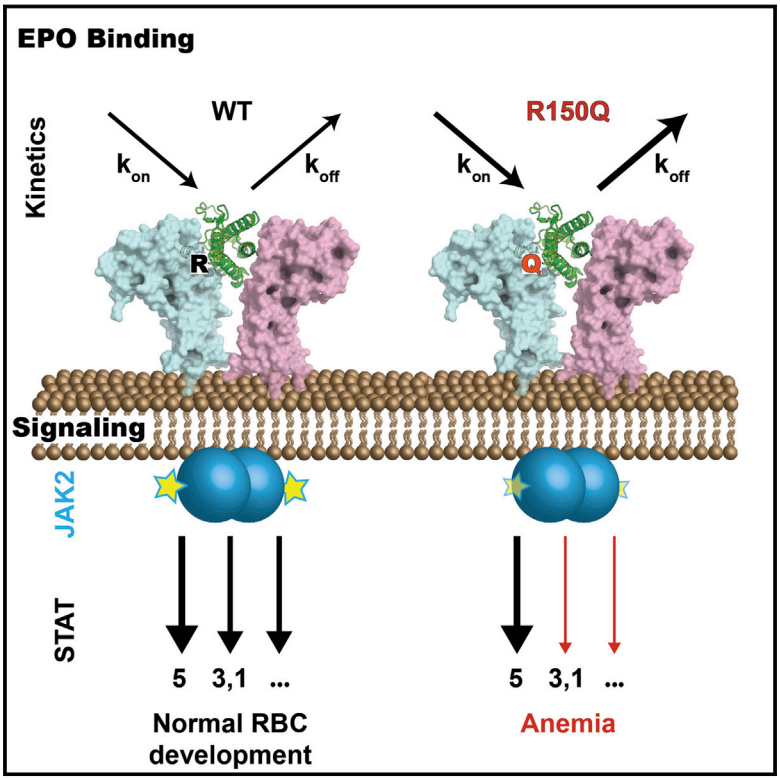

Highlights

- An anemia-associated *EPO* mutation alters the kinetics of receptor binding
- Extracellular binding changes result in biased downstream signaling responses
- The EPO variant shows that functional selectivity is possible in cytokine signaling
- Exome sequencing and follow-up studies lead to successful therapy for a rare anemia

Authors

Ah Ram Kim, Jacob C. Ulirsch, Stephan Wilmes, ..., Hanna T. Gazda, Daryl E. Klein, Vijay G. Sankaran

Correspondence

daryl.klein@yale.edu (D.E.K.), sankaran@broadinstitute.org (V.G.S.)

In Brief

A disease-causing mutation in erythropoietin surprisingly causes only a mild change in the affinity for its receptor, but alters extracellular binding kinetics, thereby affecting downstream signaling.

Kim et al., 2017, Cell *168*, 1053–1064
March 9, 2017
http://dx.doi.org/10.1016/j.cell.2017.02.026

CellPress

Article

Cell

Functional Selectivity in Cytokine Signaling Revealed Through a Pathogenic *EPO* Mutation

Ah Ram Kim,[1,2,3] Jacob C. Ulirsch,[1,2,3] Stephan Wilmes,[4] Ekrem Unal,[5] Ignacio Moraga,[6] Musa Karakukcu,[5] Daniel Yuan,[7] Shideh Kazerounian,[7] Nour J. Abdulhay,[1,2,3] David S. King,[8] Namrata Gupta,[3] Stacey B. Gabriel,[3] Eric S. Lander,[3] Turkan Patiroglu,[5] Alper Ozcan,[5] Mehmet Akif Ozdemir,[5] K. Christopher Garcia,[6] Jacob Piehler,[4] Hanna T. Gazda,[3,7] Daryl E. Klein,[9,*] and Vijay G. Sankaran[1,2,3,10,*]

[1]Division of Hematology/Oncology, The Manton Center for Orphan Disease Research, Boston Children's Hospital, Harvard Medical School, Boston, MA 02115, USA

[2]Department of Pediatric Oncology, Dana-Farber Cancer Institute, Harvard Medical School, Boston, MA 02115, USA

[3]Broad Institute of MIT and Harvard, Cambridge, MA 02142, USA

[4]Department of Biology, Division of Biophysics, University of Osnabrück, 49076 Osnabrück, Germany

[5]Department of Pediatrics, Division of Pediatric Hematology and Oncology, Faculty of Medicine, Erciyes University, Kayseri 38039, Turkey

[6]Department of Molecular and Cellular Physiology, Howard Hughes Medical Institute, Stanford University School of Medicine, Stanford, CA 94305, USA

[7]Division of Genetics and Genomics, The Manton Center for Orphan Disease Research, Boston Children's Hospital, Harvard Medical School, Boston, MA 02115, USA

[8]Howard Hughes Medical Institute Mass Spectrometry Laboratory, University of California Berkeley, Berkeley, CA 94720, USA

[9]Department of Pharmacology, Cancer Biology Institute, Yale University School of Medicine, West Haven, CT 06516, USA

[10]Lead Contact

*Correspondence: daryl.klein@yale.edu (D.E.K.), sankaran@broadinstitute.org (V.G.S.)

http://dx.doi.org/10.1016/j.cell.2017.02.026

SUMMARY

Cytokines are classically thought to stimulate downstream signaling pathways through monotonic activation of receptors. We describe a severe anemia resulting from a homozygous mutation (R150Q) in the cytokine erythropoietin (EPO). Surprisingly, the EPO R150Q mutant shows only a mild reduction in affinity for its receptor but has altered binding kinetics. The EPO mutant is less effective at stimulating erythroid cell proliferation and differentiation, even at maximally potent concentrations. While the EPO mutant can stimulate effectors such as STAT5 to a similar extent as the wild-type ligand, there is reduced JAK2-mediated phosphorylation of select downstream targets. This impairment in downstream signaling mechanistically arises from altered receptor dimerization dynamics due to extracellular binding changes. These results demonstrate how variation in a single cytokine can lead to biased downstream signaling and can thereby cause human disease. Moreover, we have defined a distinct treatable form of anemia through mutation identification and functional studies.

INTRODUCTION

The majority of receptor signaling pathways are generally thought to function through a simple model of activation, which then promotes downstream signal propagation by a variety of distinct mechanisms (Lemmon and Schlessinger, 2010; Spangler et al., 2015). For G protein-coupled receptors (GPCRs), groundbreaking insight from human physiologic and pharmacologic responses has revealed the existence of functional selectivity (or, biased agonism), whereby a single receptor is capable of variable activation of distinct downstream pathways in response to different ligands (Kenakin, 2011; Wisler et al., 2014). The extent to which other receptor signaling pathways utilize such functional selectivity in physiologic settings remains unclear, particularly for receptor signaling systems that require either homo- or hetero-dimerization for activation. Such signaling systems include receptor tyrosine kinases and cytokine receptors (Kovacs et al., 2015; Kovanen and Leonard, 2004; Lemmon et al., 2016; Lemmon and Schlessinger, 2010; Spangler et al., 2015). Recent studies have shown that engineered bivalent antibody fragments can display biased agonism through altered geometry of cytokine receptor interactions (Moraga et al., 2015b). Moreover, subtypes of cytokine classes, such as type I interferons, which signal through a common set of receptors, display selectivity toward specific physiologic responses as a result of alterations in receptor-ligand binding affinities (Spangler et al., 2015; Thomas et al., 2011; Wilmes et al., 2015). How signals from other natural ligands are tuned in this way remains largely unexplored, however, as do the in vivo consequences of variable activation of specific signaling pathways downstream of cytokines.

In the context of GPCRs, functional selectivity (or, biased agonism) has been shown to arise from alteration of equilibrium binding affinity of a ligand to its receptor or from stabilization of particular receptor conformations as a result of ligand binding (Kenakin, 2011; Manglik et al., 2015; Wisler et al., 2014). A variety of analytic methods have been developed to formalize this concept and primarily rely upon the measurement of the dissociation constant that an agonist has for a particular activity

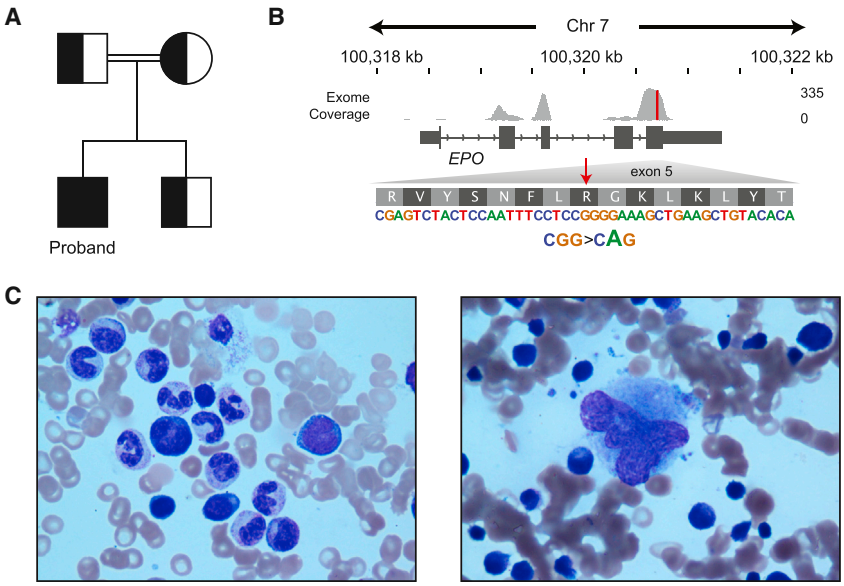

Figure 1. Autosomal Recessive Pure Red Cell Aplasia Resulting from a Homozygous *EPO* Mutation

(A) Familial segregation of an EPO mutation in a consanguineous Turkish family. All individuals had mutations confirmed by Sanger sequencing and the inheritance pattern is depicted with half-filled squares or circles indicative of heterozygous carrier status.

(B) Location of the R150Q EPO mutation in genomic sequence with exome read coverage shown. The mutation is highlighted with a red line in the exome coverage and by a red arrow in the sequence below.

(C) Bone marrow aspirate sections showing normal myeloid, lymphoid, and megakaryocyte maturation from the proband. The microscope images of the aspirate were taken with a 100× objective.

See also Figure S1.

(potency) and the maximal achievable effect downstream of a particular signaling response (efficacy) (Kenakin, 2011; Rajagopal et al., 2011). Indeed, metrics to quantify biased agonism, such as the transducer ratio, have relied upon comparisons between the efficacy and potency for a particular response (Kenakin et al., 2012). In an analogous manner with GPCRs, recent studies of cytokine signaling have shown that both alteration of ligand-receptor affinities or stabilization of alternative conformational states can lead to biased agonism (Moraga et al., 2015b; Wilmes et al., 2015). However, emerging evidence suggests that kinetic parameters may also have a key role in determining the extent of biased agonism observed in GPCR signaling (Klein Herenbrink et al., 2016). Here, through the investigation of rare experiments of nature, we uncover a cytokine-receptor binding kinetic mechanism that alters receptor dimerization dynamics and causes biased downstream signaling by JAK2. Additionally, the insight gained through these functional studies has allowed us to successfully apply recombinant cytokine therapy in a patient with a rare mutation affecting cytokine signaling.

RESULTS

Identification of an *EPO* Mutation Causing Hypoplastic Anemia

While attempting to identify previously unknown genetic etiologies causing Diamond-Blackfan anemia (DBA) (Danilova and Gazda, 2015; Landowski et al., 2013; Sankaran et al., 2012)—a disorder where red blood cell production is impaired due to a selective absence of erythroid precursors and progenitors in the bone marrow—we encountered the case of a 6 year old male child of a first-cousin consanguineous union who was diagnosed at 1 year of age with DBA and required regular transfusions. The child was started on and responded to corticosteroids at 1.5 years of age, but severe steroid-induced osteopenia necessitated transitioning back to a chronic transfusion regimen 1 year later. When the child was 6 years of age, a decision was made to proceed with a bone marrow transplant from a fully human leukocyte antigen (HLA)-matched maternal aunt. Despite the achievement of full donor chimerism, the patient continued to require packed red blood cell transfusions. Gastrointestinal graft versus host disease occurred soon after chimerism was achieved, and by day 150 following the transplant, the patient developed capillary leak syndrome and passed away of resultant complications.

Despite the typical clinical and pathologic appearance of DBA (Figure 1C, Figure S1), a number of features made this case unusual. First, stem cell transplantation in DBA normally cures the anemia once donor chimerism is achieved (Roy et al., 2005). Second, given that DBA is generally thought to display autosomal dominant inheritance, it was surprising to discover that the parents of the child were unaffected first cousins (Figure 1A) (Sankaran et al., 2012). Given these atypical features, whole-exome sequencing of the child was undertaken in an attempt to identify an underlying genetic etiology (Figure 1A) (Casanova et al., 2014; Sankaran et al., 2012; Sankaran et al., 2015). After filtering out common genetic variation, no potential causal mutations could be identified in genes known to cause DBA (Landowski et al., 2013; Sankaran et al., 2012). Given that the parents were first cousins and unaffected, we hypothesized that a homozygous recessive mutation might underlie the anemia. By examining candidate homozygous recessive mutations, a previously unknown homozygous mutation in *EPO* was identified (chr7:100,320,704 G>A). This mutation was absent from a cohort of 60,706 individuals depleted for Mendelian disease (Lek et al., 2016) and occurred in the heterozygous state in the unaffected sibling and parents, fitting the model of complete penetrance for an autosomal recessive mutation (Figures 1A and 2B, Tables S1, S2, and S3). The identified missense variant would result in substitution of glutamine for arginine at position 150 of the mature erythropoietin (EPO) protein (herein R150Q). Curiously, when EPO levels were measured while the patient was on regular transfusions (which will suppress the production of EPO), they were noted to be over 100-fold

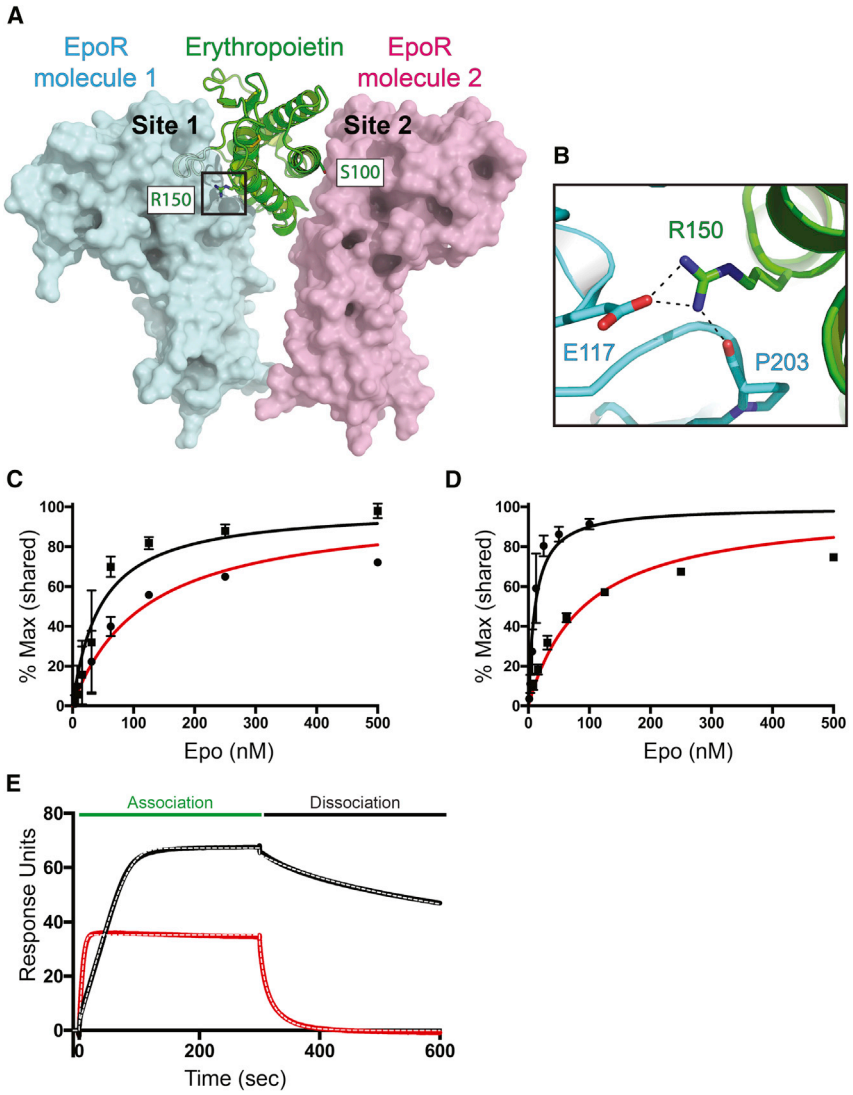

Figure 2. Alteration of EPO Receptor Binding Kinetics by the R150Q Mutation

(A) The structure of the EPO receptor (EPOR) asymmetric dimer is shown with the regions on site 1 and site 2 highlighted in the structure. The R150 and S100 residues that were mutated are shown at these sites.

(B) A zoomed in view of the structure shows salt bridges formed between the R150 residue on EPO and the side chains on site 1 of EPOR (show in blue).

(C) Concentration dependent binding of EPO wild-type (WT) and R150Q mutant to immobilized EPOR are shown in black and red, respectively. The binding was measured using surface plasmon resonance. Means ± SEM for four independent experiments are shown.

(D) Concentration dependent binding of EPO wild-type (WT) and R150Q mutant in the background of the site 2 S100E mutation to immobilized EPOR are shown in black and red, respectively. The binding was measured using surface plasmon resonance. Means ± SEM for two independent experiments are shown.

(E) Surface plasmon resonance traces at concentrations of 50 nM for WT and 62.5 nM for R150Q EPO in the S100E mutated background are shown in black and red, respectively, with an overlying 1:1 kinetic fit shown with white dotted lines. Association and dissociation phases are indicated.

See also Figure S2.

elevated (767 mU/mL; normal range of 3.5–17.6 mU/mL), suggesting that appropriate and elevated levels of the mutant EPO could be achieved.

The EPO R150Q Variant Primarily Alters Ligand-Receptor Binding Kinetics

Prior literature has shown the importance of the R150 residue in mediating interactions at the high affinity binding site (site 1) on the EPO receptor (EPOR) (Figures 2A and 2B) (Bunn, 2013; Elliott et al., 1997; Syed et al., 1998; Wen et al., 1994). Although mutations of the R150 site have been noted to mildly impair binding, the precise phenotypic effects of such mutations have not been examined in greater detail (Bunn, 2013). To directly assess the effect of this mutation, we produced recombinant wild-type (WT) and mutated EPO. The EPO variant was well expressed and behaved similarly to the WT version (Figure S2A). Electrospray mass spectrometry confirmed the purity and normal glycosylation pattern of the mutant (Figure S2B). EPO R150Q was capable of forming a complex with EPOR of comparable stability to the WT when assessed by multi-angle light scattering coupled to size exclusion chromatography (SEC-MALS) (Figures S2C and S2D). This finding suggested that there was likely a comparable affinity between EPOR and both the WT and R150Q forms of EPO. However, we could not obtain a precise measurement of affinity with SEC-MALS and therefore turned to surface plasmon resonance (Jenni et al., 2015; Moraga et al., 2015b), which revealed the mutated EPO had a dissociation constant (K_D) that was reduced by only ~3-fold (Table S4, Figure 2C). It was therefore surprising that the elevated serum EPO levels in the patient could not compensate for this mildly reduced affinity. Since binding kinetics could not readily be determined given the multi-site interaction of EPO and EPOR, we mutated the low affinity binding site of EPO (site 2, S100E mutation) (Figure 2A) (Bunn, 2013; Elliott et al., 1997; Syed et al., 1998). By comparing the WT and R150Q-mutated EPO in the S100E background (allowing only site 1 interactions), we could show that the K_D of site 1 binding was reduced 8-fold in the R150Q mutant (Figure 2D, Table S4). Interestingly, the R150Q mutation resulted in a 12-fold faster on-rate (k_{on}), as well as a 233-fold faster off-rate (k_{off}) (Figure 2E, Figure S2E, Table S4). These findings demonstrate that the R150Q mutation only mildly affects the overall affinity, but significantly alters the kinetics of the cytokine's interaction with EPOR, which could have

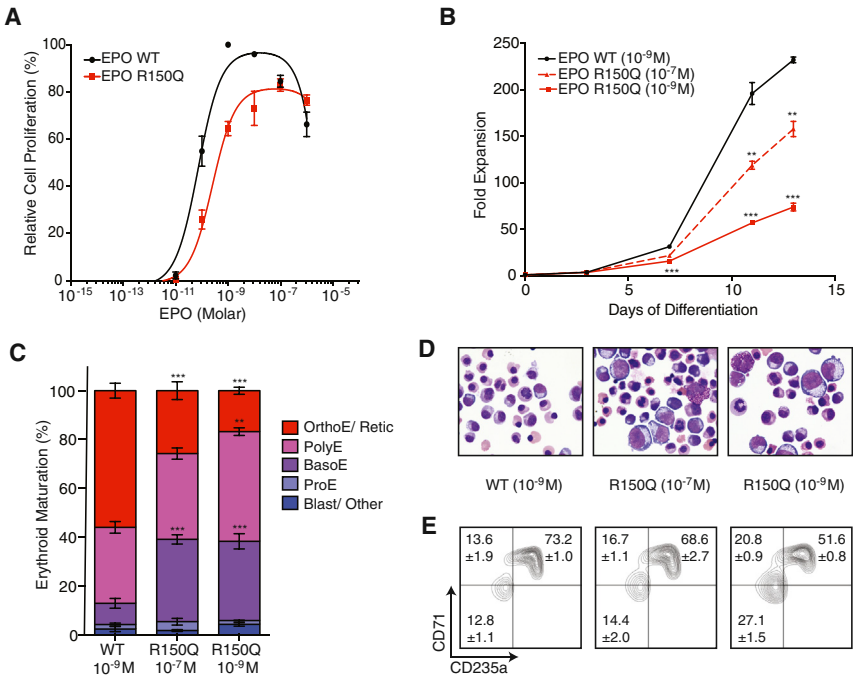

Figure 3. The EPO R150Q Mutant Impairs Erythroid Cell Proliferation and Differentiation

(A) Proliferation curves of UT7 cells after 3 days in culture are shown. Means ± SEM for three independent experiments are shown. Sigmoidal fit curves are shown.

(B) CD34+ HSPC cell growth during erythroid differentiation is shown. Means ± SEM for 3 independent experiments are shown. $^{**}p < 0.01$, $^{***}p < 0.001$ as determined by the two-tailed Student's t test. At day 7, both R150Q mutant concentrations have a $p < 0.001$ compared to the WT.

(C) Erythroid maturation at different stages assessed from cultures on day 11 of erythroid differentiation. Orthochromatic (OrthoE), polychromatic (PolyE), basophilic (BasoE), or pro-erythroblasts (ProE) were measured. Blasts and other myeloid cells were counted together. Reticulocytes were counted with OrthoEs. Means ± SEM for counts from five independent high power fields are shown. $^{**}p < 0.01$, $^{***}p < 0.001$ as determined by the two-tailed Student's t test.

(D) Representative cytocentrifugation images at 100× magnification are shown at day 11 of erythroid differentiation.

(E) Flow cytometric assessment of erythroid differentiation with the markers CD71 and CD235a at day 7 of differentiation. Means ± SEM for three independent experiments are shown.

See also Figure S3.

important consequences for downstream signaling by analogy with other receptor systems (Klein Herenbrink et al., 2016; McKeithan, 1995).

Increased Concentrations of EPO Mutant Cannot Overcome Impaired Erythropoiesis

Since the R150Q mutation appeared to alter erythropoiesis in vivo, we examined its effects on erythroid cells in vitro to gain further insight into how it causes disease. We assessed the overall proliferative response of the human erythroid cell line, UT7 (Moraga et al., 2015b), to the EPO variant and found that the potency for maximal proliferation was reduced by ~100-fold for R150Q EPO (from 10^{-9} M to 10^{-7} M), while overall efficacy was also reduced by 20% ($p = 0.00068$, Figure 3A). This observation suggested that even at concentrations of ligand demonstrating maximal potency (i.e., 10^{-7} M), the mutated EPO cannot achieve the same effect on cell proliferation as is obtained with WT EPO—implying that when the R150Q EPO concentration is increased to account for affinity loss (as in the patient), it still cannot properly stimulate erythropoiesis. Using the S100E EPO variants, we further demonstrated that the interaction of site 2 was absolutely required to mediate the proliferative response in these cells (Figure S3A).

We then turned to primary human $CD34^+$ hematopoietic stem and progenitor cells (HSPCs), which can be cultured with specific cytokines over multiple phases to induce differentiation into mature red blood cells, closely mimicking multiple features of endogenous in vivo erythropoiesis (Giani et al., 2016; Ludwig et al., 2014; Ulirsch et al., 2016). At equimolar concentrations of EPO (10^{-9} M), the R150Q mutant failed to support normal erythroid expansion or differentiation, as documented by a significant reduction in growth, impaired maturation, and outgrowth of non-erythroid cells (Figures 3B–3E, Figures S3B–S3D). Even at concentrations where its maximal measured potency was achieved (10^{-7} M), R150Q-mutated EPO was impaired in its ability to promote erythroid expansion or maturation of the HSPCs (Figures 3B–3E, Figures S3C and S3D). Thus, simply adding R150Q-mutated EPO at higher concentrations to overcome its slight affinity defect does not allow it to behave like the WT ligand. In tandem with the results from the UT7 erythroid cells, these observations suggest that biased or partial activation of downstream pathways might underlie the pathology of the R150Q EPO mutation.

Biased Agonism of Select Downstream Effectors by EPO R150Q

A major downstream effector of EPO signaling is the transcription factor STAT5, which is phosphorylated by the EPOR-associated tyrosine kinase, JAK2, and localizes to the nucleus in erythroid cells after stimulation with EPO (Bunn, 2013; Giani et al., 2016; Kuhrt and Wojchowski, 2015). We measured the dosage-dependent response of STAT5 phosphorylation to either WT or R150Q-mutated EPO in erythroid cells. Consistent with the effects observed for proliferation in these cells, over the course of 30 min there was a comparable dose response with maximal potency of phosphorylation achieved at 10^{-9} M for WT and 10^{-7} M for R150Q-mutated EPO (Figure 4A). The difference in maximal normalized levels of STAT5 phosphorylation was less than 2%, and there was no difference between the absolute levels of STAT5 phosphorylation ($p = 0.938$, Figure S4A).

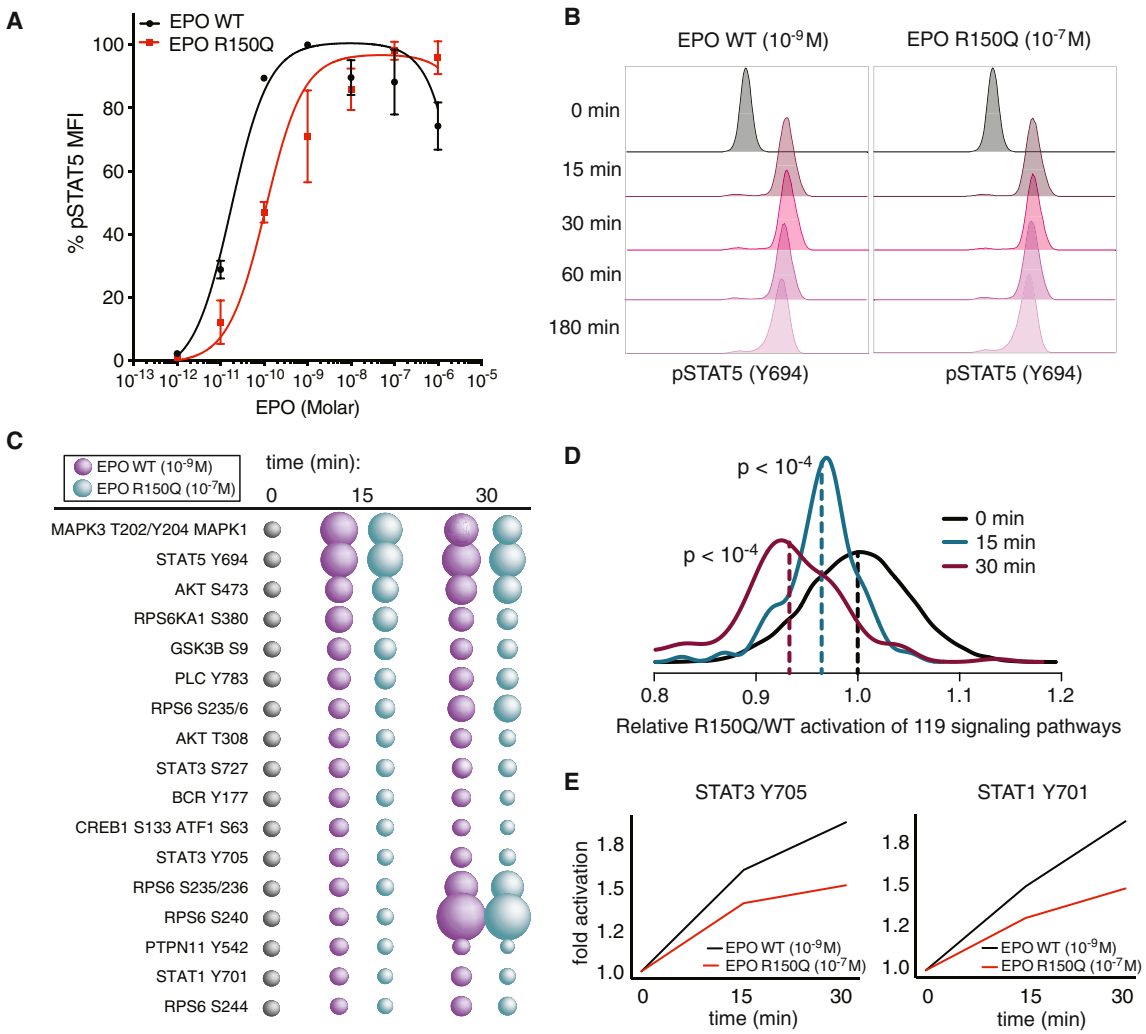

Figure 4. Functional Selectivity in EPO Signaling Revealed by the R150Q Mutant

(A) Percent of STAT5 phosphorylation (pSTAT5) as assessed by intracellular FACS mean fluorescence intensities (MFI) in UT7 cells stimulated for 30 min. Means ± SEM for three independent experiments are shown at each concentration. Sigmoidal fit curves are shown.

(B) Time dependent representative histogram plots of pSTAT5 are shown. No significant differences in replicate samples could be identified between the mutant and WT EPO at maximally potent concentrations.

(C) Signaling pathways activated (> 50% fold) by either EPO WT or R150Q in UT7 cells within 30 min of stimulation.

(D) Kernel densities of signaling across all tested pathways are shown for each time point. The unstimulated distribution (0 min) is estimated as a normal distribution with a mean of 1.0 and a SD of 0.05. P values were determined from 20,000 permutations by randomly swapping EPO WT and R150Q labels and comparing means.

(E) At 15 min, the top two most differentially activated residues are STAT3 Y705 and STAT1 Y701.

See also Figure S4.

The time-dependent stimulation of STAT5 phosphorylation largely overlapped, with peak stimulation observed at 15 min (Figure 4B, Figure S4B). Given that STAT5 phosphorylation was observed to be similar at maximally potent concentrations, this suggested that other downstream targets might show biased activation in this setting, arising from the different binding kinetics of R150Q EPO. A recent analysis of engineered synthetic ligands for EPOR has demonstrated that biased signaling can be detected by broadly surveying a panel of phosphorylated substrates (Moraga et al., 2015b). We therefore undertook an intracellular flow cytometric analysis of such phosphorylated substrates in erythroid cells stimulated with either WT or R150Q-mutated EPO at maximally potent concentrations (10^{-9} M for WT and 10^{-7} M for R150Q) (Krutzik et al., 2011). Although many major targets—like STAT5— showed similar profiles for both EPO ligands (Figure 4C), a subset of targets showed altered activation (Tables S5 and S6). Indeed, the overall profile of activation was shifted as a result of this subset of targets having reduced phosphorylation due to the R150Q mutant (Figure 4D). The phosphorylation of STAT1 and STAT3, which are both activated downstream of EPO (Moraga et al., 2015b), were the most significantly impaired targets (at both 15 and 30 min time points)

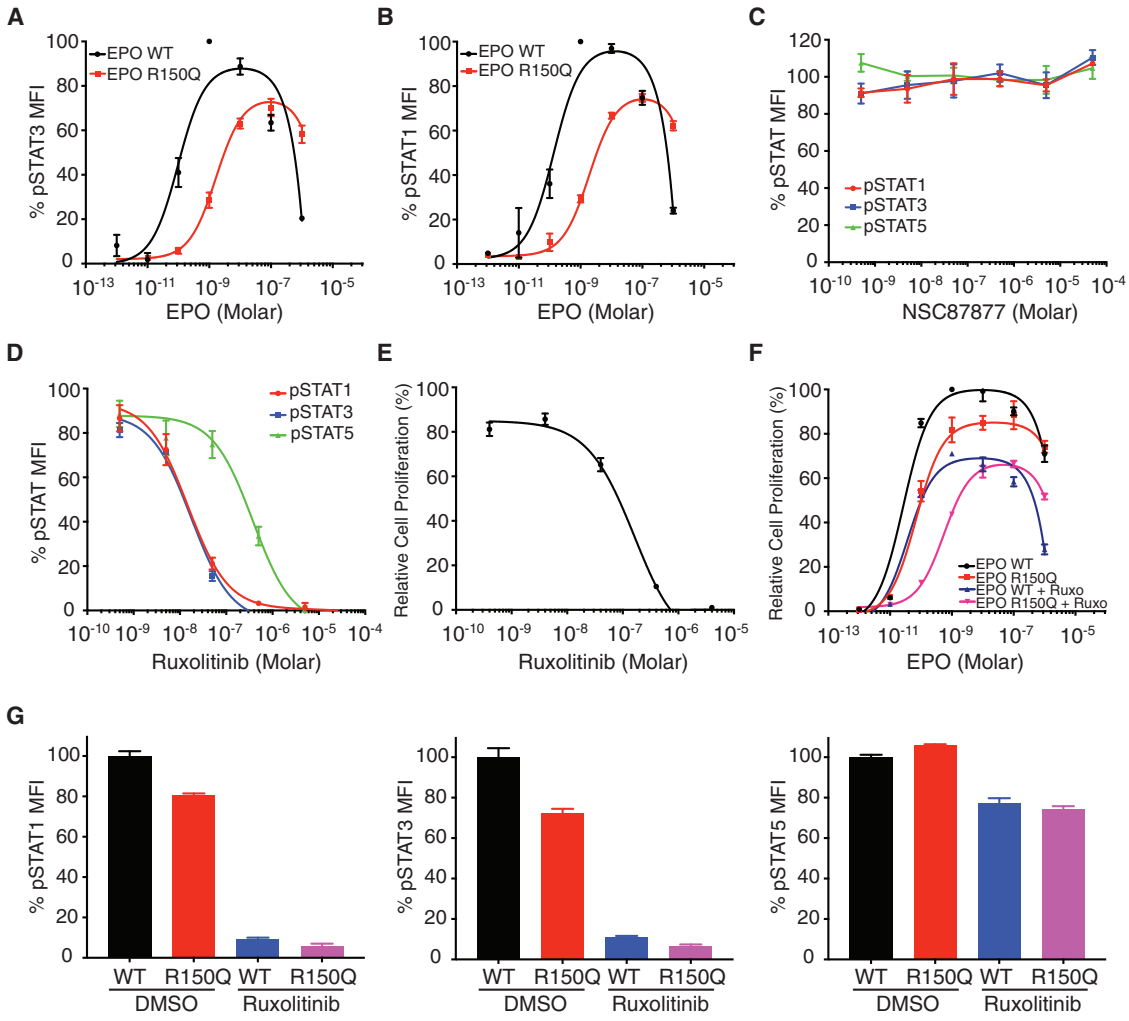

Figure 5. Biased Agonism of the R150Q EPO Mutation Arises Due to Impaired JAK2 Activation

(A and B) Percent of STAT3 and STAT1 phosphorylation (pSTAT3 and pSTAT1, respectively) as assessed by intracellular FACS in UT7 cells stimulated for 30 min with either the R150Q or WT EPO. Mean ± SEM for 3-4 independent experiments are shown at each concentration. Sigmoidal fit curves are shown.

(C) Percent of pSTAT1/3/5 in UT7 cells following treatment with NSC87877 (SHP1/2 inhibitor). Mean ± SEM for 3 independent experiments are shown at each concentration. The 100% level of phosphorylation is based on assessment of untreated samples.

(D) Percent of pSTAT1/3/5 in UT7 cells following treatment with ruxolitinib (JAK2 inhibitor). Mean ± SEM for 3 independent experiments are shown at each concentration. The 100% level of phosphorylation is based on assessment of untreated samples. Sigmoidal fit curves are shown.

(E) Proliferation curves of UT7 cells of with various concentrations of ruxolitinib with EPO WT (10^{-9}M) after 3 days in culture are shown. Means ± SEM for three independent experiments are shown. A sigmoidal fit curve is shown.

(F) Proliferation curves of UT7 cells at different concentrations of EPO WT or R150Q either in the presence of vehicle (DMSO) or ruxolitinib (Ruxo, 40 nM) after 3 days in culture are shown. Means ± SEM for three independent experiments are shown. Sigmoidal fit curves are shown.

(G) Percent of pSTAT1/3/5 in UT7 cells treated with or without a low dose of ruxolitinib (40 nM) and with maximally potent concentrations of either the WT (10^{-9} M) or R150Q mutated EPO (10^{-7} M). Means ± SEM for three experiments are shown.

See also Figure S5.

at maximally potent concentrations (10^{-7} M) of the R150Q EPO (Figure 4E).

Impaired JAK2 Activation Underlies Biased Agonism of EPO R150Q

STAT1 and STAT3 phosphorylation were reduced across a range of EPO R150Q concentrations and, in contrast to STAT5, never reached the same extent of activation, even at maximally potent concentrations of the mutated EPO (Figures 5A and 5B). There was a 25%–30% reduction in the phosphorylation of STAT1 and STAT3 at maximally potent concentrations of the R150Q as compared with the WT EPO ligand ($p = 0.00016$ and 0.00027 for STAT1 and STAT3, respectively). These results could be recapitulated by western blotting (Figures S5A and S5B), substantiating the findings from intracellular flow cytometry. Similar results were also observed in primary human

erythroid cells (Figure S5C). To define whether STAT1 and STAT3 were necessary for EPO-induced erythroid cell proliferation, we targeted these two factors separately or in tandem with short hairpin RNAs and noted a reduction in cell proliferation in UT7 cells in all cases (Figure S5D). Importantly, the targeted STAT was consistently suppressed (Figures S5E–S5G). Interestingly, even with short-term suppression (over the course of days), other STATs were noted to change in expression, consistent with compensatory responses. In cultures of HSPCs differentiating toward the erythroid lineage, there was decreased growth and mildly impaired differentiation (as evident from an accumulation of $CD235a^{-}/CD71^{-}$ non-erythroid cells) with suppression of STAT1, STAT3, or both proteins (Figures S5H and S5I). These results are supported by prior studies in human erythroid cells and mice in vivo, demonstrating the importance of these distinct pathways in EPO signaling (Halupa et al., 2005; Kirito et al., 2002; Kirito et al., 1997). We would note that although decreased STAT1 and STAT3 activation might underlie some of the observed phenotypes with the R150Q EPO, they are unlikely to be the sole effectors resulting in the observed impairment in erythropoiesis. Impaired activation of other pathways, such as RAS-MAP kinase signaling, might additionally contribute to the observed phenotypes (Figure 4C) (Kuhrt and Wojchowski, 2015).

The dramatic reduction in the phosphorylation of STAT1 and STAT3, but not of STAT5, downstream of this mutated ligand suggested that either an upstream activator or a downstream regulator of STAT phosphorylation was affected by the mutant ligand. We reasoned that understanding the basis for this biased agonism of specific downstream effectors could provide mechanistic insight into the underlying altered activity of the mutated EPO. STAT transcription factors are dephosphorylated by the phosphatases SHP-1 (PTPN6) and SHP-2 (PTPN11) (Chen et al., 2003; Wu et al., 2002; Yu et al., 2000). We utilized a selective inhibitor of SHP-1 and SHP-2, NSC-87877 (Chen et al., 2006), and observed no major change in EPO-induced STAT1, STAT3, or STAT5 phosphorylation in the erythroid cells at various doses (Figure 5C), suggesting that the activity of these phosphatases was unlikely to underlie the observed bias in the pattern of STAT phosphorylation.

Variation at the level of upstream activity therefore appeared more likely to be responsible for the selective activation of downstream effectors. Ligand-induced dimerization of the EPOR results in activation of the associated tyrosine kinase JAK2, which in turn is able to directly phosphorylate the STAT transcription factors (Bunn, 2013; Kuhrt and Wojchowski, 2015; Moraga et al., 2015b; Spangler et al., 2015). We suppressed JAK2 activity with the specific kinase inhibitor ruxolitinib and examined the activation of the three STAT transcription factors (Quintás-Cardama et al., 2010; Tefferi, 2012). Surprisingly, we observed biased antagonism when we suppressed EPO-stimulated JAK2 activation (Figure 5D). There was a greater than 20-fold difference in the potency of ruxolitinib inhibition of STAT1 and STAT3 phosphorylation (IC_{50} of 1.3×10^{-8} M), as compared with STAT5 phosphorylation (IC_{50} of 2.8×10^{-7} M) (Figure 5D). Such biased antagonism by ruxolitinib has only rarely been reported (Tefferi, 2012).

We saw reduced proliferation of the erythroid cells at ruxolitinib concentrations that would impair STAT1 and STAT3, but not STAT5, phosphorylation (e.g., 4×10^{-8} M) (Figure 5E), similar to what was observed for the R150Q EPO mutant (Figure 3A). This demonstrates that an impairment in erythroid cell proliferation and STAT1 and STAT3 phosphorylation is observed with both the kinetically-biased EPO mutant or with low-level JAK2 inhibition. We could obtain similar results as observed for ruxolitinib using another specific and mechanistically distinct JAK2 inhibitor, CHZ868 (Figures S5J and S5K) (Meyer et al., 2015). These observations suggested that the functional selectivity of the EPO R150Q mutant could be due to impaired JAK2 activation. To directly test this, we added low dose (4×10^{-8} M) ruxolitinib to varying concentrations of either the R150Q-mutated or WT EPO. The selective inhibition of JAK2 resulted in a similar maximal efficacy of erythroid cell proliferation for the R150Q and WT forms of EPO (Figure 5F, Figure S5L). Importantly, treatment with this low dose of ruxolitinib dramatically reduced phosphorylation of STAT1 and STAT3 to similar levels with maximally potent concentrations of either the WT or R150Q EPO ligands, while minimally affecting STAT5 phosphorylation levels (Figure 5G). These results demonstrate that the impaired erythropoiesis and functional selectivity of the R150Q EPO are due to impaired JAK2 activation. If JAK2-independent pathways were playing additional roles in the impaired activation downstream of the R150Q EPO mutant, a sizable residual difference should be seen in the maximal erythroid cell proliferation after ruxolitinib treatment. However, this was not the case (difference of <7%, $p = 0.065$; Figure S5L), and thus JAK2 activation appeared to be a primary mediator of the impaired erythropoiesis due to the R150Q-mutated EPO.

Altered EPOR Dimerization Dynamics Limit JAK2 Activation by EPO R150Q

We have shown that the EPO R150Q mutation, which was identified in a patient with congenital hypoplastic anemia, alters the kinetics of ligand-receptor binding but has only a moderate effect on the overall binding affinity. Despite having elevated EPO levels, the patient was unable to compensate for the impaired erythropoiesis present, demonstrating that this mutant alters the properties of EPO signaling. We have further shown that this kinetically-biased mutant form of EPO results in skewed activation of downstream signaling due to impaired JAK2 activity. However, the exact mechanism by which the alterations of ligand-receptor binding result in impaired JAK2 activation remain unclear.

Recent studies have demonstrated the value of using total internal reflection fluorescence (TIRF) microscopy of labeled receptor molecules on the cell surface to visualize cytokine receptor dimerization dynamics and activation (Moraga et al., 2015a; Moraga et al., 2015b; Wilmes et al., 2015). We reasoned that probing the assembly of EPOR at the single molecule level could provide insight into mechanisms underlying the altered activity of the R150Q EPO mutant. We utilized cells stably expressing EPOR, N-terminally tagged with a meGFP, which was rendered non-fluorescent (by the Y67F mutation). This tag (mXFP) is recognized by dye-conjugated anti-GFP nanobodies, allowing quantitative fluorescence labeling of EPOR at the cell surface

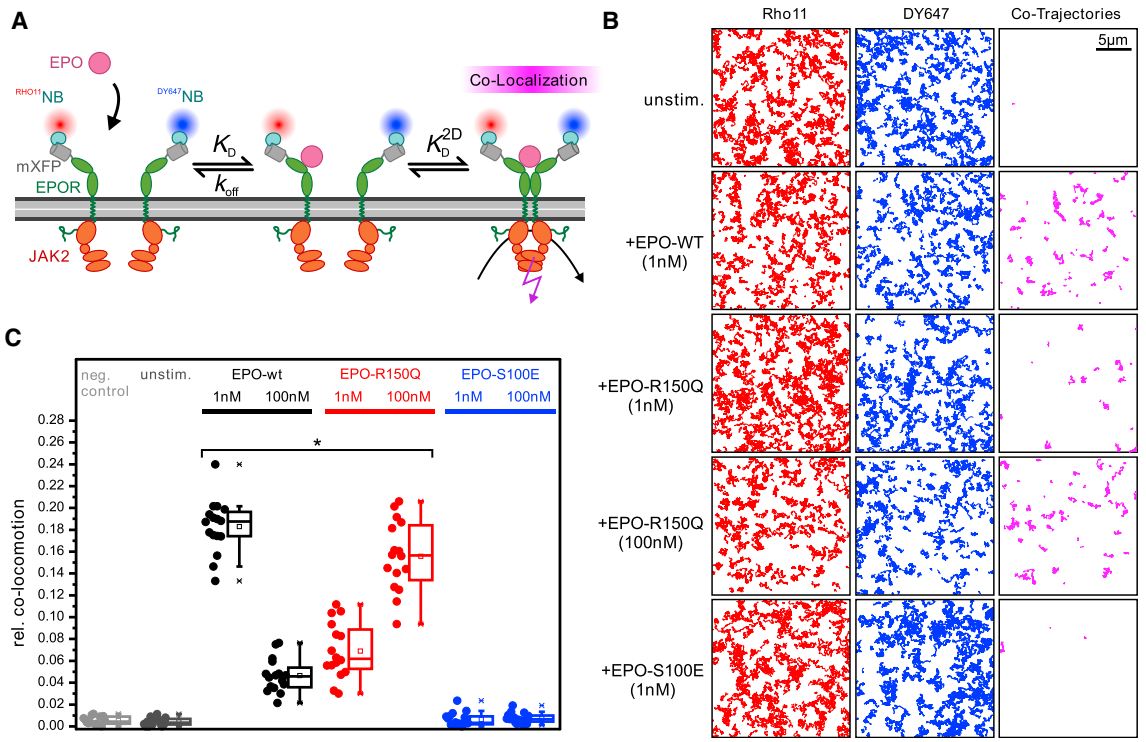

Figure 6. Dimerization of EPOR at the Cell Surface is Impaired for Mutant EPO

(A) Model of assembly and cell-surface labeling of EPOR using dye-conjugated anti-GFP nanobodies.

(B) Trajectories (150 frames, ~4.8 s) of individual RHO11-labeled (red) and DY647-labeled EpoR (blue) and co-trajectories (magenta) for unstimulated cells, as well as after stimulation with indicated EPO mutants and concentrations.

(C) Relative amount of co-trajectories for unstimulated EPOR and after stimulation with indicated EPO mutants and concentrations. Boxplots indicate the data distribution of the second and third quartile (box), median (line), mean (open squares), and whiskers (1.5× interquartile range). A comparison between maximally potent concentrations of EPO WT and R150Q is shown. *p = 0.012.

See also Figure S6.

of live cells. Well-balanced dual-color labeling was achieved using equal concentrations of nanobodies either conjugated with RHO11 or with DY647 (Moraga et al., 2015b; Wilmes et al., 2015). JAK2 was co-expressed in order to ensure full functionality and expression of the receptor system (Huang et al., 2001).

We used dual-color TIRF imaging to visualize the spatiotemporal dynamics of EPOR after exposure to different concentrations of either the WT or mutant EPO ligands (Figure 6A, Figure S6, Movie S1). Single-molecule co-localization and co-tracking analysis was used to identify correlated motion (co-locomotion) of the spectrally separable fluorescent molecules, which was taken as readout for productive dimerization of EPOR. In the absence of stimulation, there was very little dimerization observed, which could be increased significantly upon stimulation with maximally potent concentrations of WT EPO (Figures 6B and 6C). This observation strongly supports the concept that the EPO ligand induces dimerization of EPOR and thus results in downstream activation through this mechanism (Moraga et al., 2015b) (Figure 6B). When we examined the R150Q mutant, we noted consistently reduced levels of dimerization, even at maximally potent concentrations (100 nM ligand) (Figure 6C). The extent of dimerization was on average 1.2-fold reduced ($p = 0.012$) as compared to the WT at maximally potent concentrations (1 nM). Importantly, excess levels of the WT EPO (100 nM) impaired dimer formation, given that high affinity interactions with receptors are favored over the formation of an EPOR dimer complex at such high ligand concentrations. Consistent with this observation, the S100E EPO, which only has an intact site 1 for EPOR, but cannot bind to the lower affinity site (site 2), failed to elicit dimerization even at high concentrations of ligand (Figure 6C). Collectively, these results show that the R150Q mutant has a reduced ability to promote EPOR dimer formation, resulting in reduced JAK2 activation even at maximally potent concentrations. Formation of such EPOR dimers is critical for the full activation of JAK2 (Silvennoinen and Hubbard, 2015). Despite an increase in concentration to overcome any affinity deficit, the R150Q EPO failed to induce maximal receptor dimerization and proper signaling. Our observations demonstrate that ligand-receptor binding kinetics can affect receptor dimerization dynamics on an intact cell surface, and this in turn can modulate downstream signal transduction.

Therapeutic Intervention in a Patient with the EPO R150Q Mutation

Our study that began with the analysis of a rare patient has revealed how tuning of downstream signaling responses could

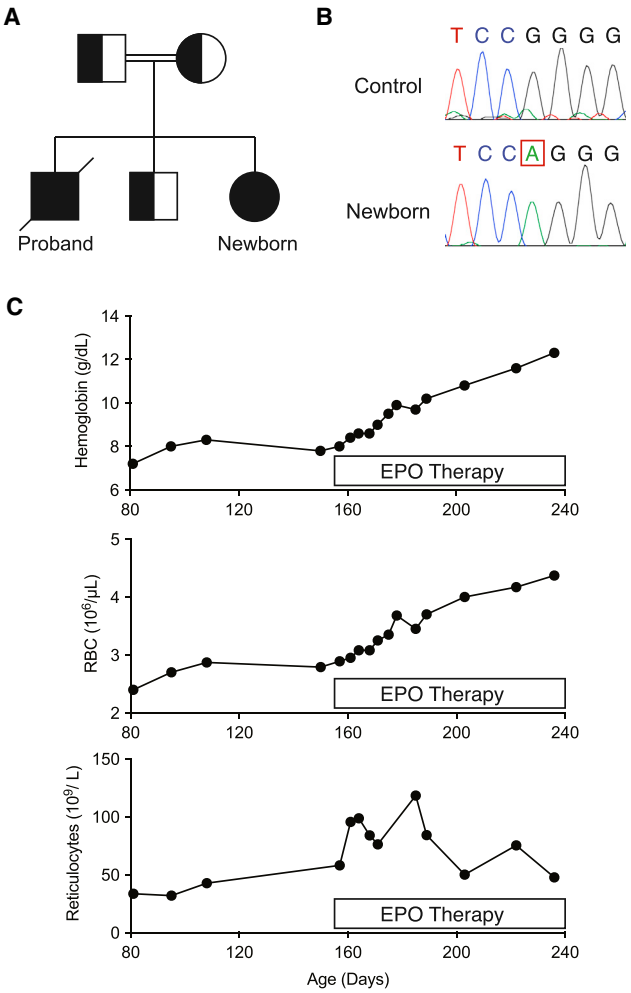

Figure 7. Recombinant Cytokine Therapy in an Infant with the EPO R150Q Mutation

(A) Updated pedigree of the family examined here after the birth of an infant affected with reticulocytopenic anemia (please note that the proband had passed away of bone marrow transplant related complications prior to the birth of this child).

(B) Sanger sequence traces showing the presence of the homozygous mutation in the *EPO* gene (chr7:100,320,704 G>A) in the newborn infant sibling of the proband and a control healthy donor control. Sequencing was also re-confirmed in DNA samples from all family members.

(C) Time dependent changes in hemoglobin levels, RBC counts, and reticulocyte counts in the affected infant sibling of the proband (newborn). The x axis shows the infant's age in days. The box highlighting recombinant EPO therapy begins at day of life 153, when the first injection of this medication was given subcutaneously to the patient.

be achieved through kinetic changes in cytokine-receptor interactions. Unfortunately, the proband identified with the EPO R150Q mutation passed away prior to mutation identification, as a result of complications stemming from the bone marrow transplantation procedure. While this work was undergoing revision, the parents of the proband had another child. Similar to the proband, this newborn infant was noted to be anemic, with a hemoglobin of ~7 g/dL and an inappropriately low reticulocyte response, even after the period of the normal physiologic newborn nadir (Sankaran and Agrawal, 2013). In addition, multiple measurements of serum EPO levels showed significantly elevated levels (>750 mU/mL at 108 and 150 days of life) without an appropriate erythropoietic response. Confirmatory sequencing revealed that this newborn infant also harbored the homozygous variant in *EPO* (chr7:100,320,704 G>A), resulting in the R150Q mutation (Figures 7A and 7B). As a result, after appropriate permissions were obtained, a trial of recombinant EPO therapy was initiated (given at 50 units/kg/dose, three times a week). Since WT EPO should be able to readily compete with the R150Q mutant, as occurs in the heterozygous parents and sibling, we expected that recombinant EPO therapy should work in this patient. While treatment has only been performed over the course of eleven weeks, the child has shown a robust and appropriate reticulocyte response, with a steady rise in hemoglobin levels into the normal range (Figure 7C). Without such therapy, it is very likely that the anemia would have progressively worsened and would have likely necessitated initiation of transfusion therapy, as occurred in the elder sibling of this infant and as is often seen in other cases of congenital anemia. Importantly, recombinant EPO therapy has been trialed in DBA patients previously with no response noted (Narla et al., 2011). Therefore, this anemia due to the EPO R150Q mutation defines a distinct treatable blood disorder.

DISCUSSION

By using both genetic and experimental studies (Casanova et al., 2014; MacArthur et al., 2014), we identified a missense variant in the *EPO* gene that results in congenital hypoplastic anemia. These rare experiments of nature illustrate how functional selectivity in receptor signaling can have important physiologic consequences and, to the best of our knowledge, provide the first examples of how this can result in human disease. Despite the ability of the proband and his sibling with the homozygous R150Q mutations to upregulate EPO production to levels that should offset induced affinity changes, these patients could not compensate for the defect in EPO signaling to enable normal erythropoiesis. Our studies show that the R150Q EPO cannot achieve the same maximal efficacy as WT EPO in terms of promoting erythroid differentiation or proliferation. Treatment with corticosteroids, which can expand early erythroid progenitors independently from EPO (Flygare et al., 2011), allowed the proband to have an improvement in the anemia, which shows that some signaling through EPOR is still possible with the R150Q mutant, as we directly demonstrate through in vitro studies. In addition, the infant sister of the proband who had a reticulocytopenic anemia demonstrated a robust hematologic response to treatment with recombinant EPO, suggesting that through the functional studies we have performed, we have been able to define a treatable form of congenital hypoplastic anemia. This provides a rare example of how whole-exome sequencing and follow-up studies can lead to successful and modified treatment approaches, as has been recently described for specific metabolic disorder cases (Tarailo-Graovac et al., 2016).

Our results are consistent with a model of altered ligand-receptor binding kinetics, resulting in impaired receptor dimerization dynamics. More rapid dissociation of the R150Q EPO ligand ($t_{1/2}$ of less than 10 s for the R150Q mutant, as compared to greater than 5 min for WT) prevents optimal EPOR signaling by restricting activation of JAK2 and thereby limiting its ability to fully activate specific downstream effectors, including STAT1 and STAT3. We observe that these particular targets are more sensitive to inhibition by the JAK2 inhibitors, ruxolitinib and CHZ868. These findings demonstrate that specific JAK2 targets can have variable propensities for phosphorylation, depending upon the extent of JAK2 activation. We show that the R150Q EPO ligand behaves as a partial agonist for JAK2 activation at maximal potency and therefore results in biased signaling. Overall, our findings from a pathologic case demonstrate a mechanism through which tuning of intracellular signaling downstream of cytokine receptors can be achieved via alteration of JAK2 activation. It is likely that other cytokine signaling systems may take advantage of such tuning mechanisms to alter downstream signaling responses (Spangler et al., 2015).

Several analyses have investigated kinetic proofreading in receptors (Klein Herenbrink et al., 2016; Lemmon et al., 2016; McKeithan, 1995; Thomas et al., 2011), and their findings suggest that productive receptor signaling can only occur if the activating ligand remains bound for sufficient time to allow the multiple steps required for downstream receptor signaling to ensue—against the background of multiple rapid inactivation steps. Our results show how this mechanism can be of relevance to EPO and other cytokine signaling pathways. Faster dissociation of the mutant ligand prevents optimal EPOR dimerization and downstream JAK2 activation, demonstrating that kinetic parameters have a key role in determining the quality of signaling achieved downstream of such receptors. An important implication of these findings is that, analogous to biased agonists identified for various GPCRs (Kenakin, 2011; Wisler et al., 2014), cytokine receptors can also display such behavior to altered ligands, and this can have important physiological consequences, as shown by the patient that led us to investigate this phenomenon. This also suggests that beyond alteration of conformation and affinity, which have previously been suggested as mechanisms for tuning cytokine signaling (Moraga et al., 2015b; Wilmes et al., 2015), kinetic parameters can have a key role in altering downstream responses.

By applying the principle of functional selectivity, it may also be possible to design agonists that achieve specific physiologic responses downstream of endogenous cytokine pathways, while avoiding other untoward effects. Thus, modification of ligand-receptor kinetic parameters could tune downstream intracellular signaling responses and lead to more effective therapeutic manipulation of cytokine signaling. Our findings stress the importance of looking at downstream signaling by using multiparameter approaches, such as through surveys of a broad array of phosphorylated proteins (Knapp et al., 2017; Krutzik et al., 2011). As in the case we have examined here, specific targets such as STAT5 show normal activation at maximally potent concentrations of the mutant ligand. However, the same extent of erythropoiesis can never be achieved with this mutant, as we show in vitro, which is completely consistent with what has been observed in vivo in the patients. Examining multiple responses allows for ascertainment of functional selectivity in such settings. Our findings that began with rare experiments of nature highlight the importance of considering both dynamic states of activation and the multidimensional nature of downstream responses in the context of cytokine signaling.

STAR★METHODS

Detailed methods are provided in the online version of this paper and include the following:

- KEY RESOURCES TABLE
- CONTACT FOR REAGENT AND RESOURCE SHARING
- EXPERIMENTAL MODEL AND SUBJECT DETAILS
  - UT7/EPO Cell Culture
  - Primary Cell Culture
- METHOD DETAILS
  - Recombinant Protein Expression and Purification
  - Mass Spectrometry
  - Surface Plasmon Resonance
  - Size Exclusion Chromatography-Multiangle Light Scattering (SEC-MALS)
  - Proliferation Assay
  - Evaluation of Erythroid Maturation
  - Flow Cytometry
  - Phosphorylated STAT Assessment with Intracellular Flow Cytometry
  - Western Blotting
  - Phosphorylated Protein Analysis
  - Viral Production and Infection
  - RNA Extraction, cDNA Synthesis, and Quantitative RT-PCR
  - Single-Molecule Tracking, Co-localization, and Co-tracking Analyses
- QUANTIFICATION AND STATISTICAL ANALYSIS
  - Single Molecule Tracking, Co-Localization and Co-Tracking Analyses
  - Statistical Analysis of Binding and Kinetic Data
  - Whole-Exome Sequencing Analysis

SUPPLEMENTAL INFORMATION

Supplemental Information includes six figures, six tables, and one movie and can be found with this article online at http://dx.doi.org/10.1016/j.cell.2017.02.026.

AUTHOR CONTRIBUTIONS

Conceptualization, A.R.K., J.C.U., E.U., H.T.G., D.E.K., and V.G.S.; Methodology, A.R.K., J.C.U., S.W., K.C.G., J.P., D.E.K., and V.G.S.; Investigation, A.R.K., J.C.U., S.W., E.U., I.M., M.K., D.Y., S.K., N.J.A., D.S.K., N.G., S.B.G., E.S.L., T.P., A.O., M.A.O., K.C.G., J.P., H.T.G., D.E.K., and V.G.S.; Writing – Original Draft, A.R.K., D.E.K., and V.G.S.; Writing – Review & Editing, A.R.K., J.C.U., S.W., E.U., I.M., E.S.L., K.C.G., J.P., H.T.G., D.E.K., and V.G.S.; Funding Acquisition, S.B.G., E.S.L., H.T.G., and V.G.S.; Resources, J.C.U., S.W., I.M., K.C.G., J.P., D.E.K., and V.G.S.; Supervision, K.C.G., J.P., H.T.G., and V.G.S.

ACKNOWLEDGMENTS

We are grateful to the family described in this paper for their willingness to participate in this study. We thank M. Lemmon, S. Harrison, H. Lodish, F. Bunn, J. Casanova, D. Nathan, S. Orkin, D. Ginsburg, and members of the Sankaran laboratory for valuable comments and advice on this work. We thank S. Ozcan for assistance with aspirate imaging. This work was funded by NIH grants R01DK103794 and R33HL120791 (V.G.S.), R01HL107558 and K02HL111156 (H.T.G), and U54HG003067 (S.B.G. and E.S.L.).

Received: August 19, 2016
Revised: November 30, 2016
Accepted: February 15, 2017
Published: March 9, 2017

REFERENCES

Bunn, H.F. (2013). Erythropoietin. Cold Spring Harb. Perspect. Med. *3*, a011619.

Casanova, J.L., Conley, M.E., Seligman, S.J., Abel, L., and Notarangelo, L.D. (2014). Guidelines for genetic studies in single patients: lessons from primary immunodeficiencies. J. Exp. Med. *211*, 2137–2149.

Chen, Y., Wen, R., Yang, S., Schuman, J., Zhang, E.E., Yi, T., Feng, G.S., and Wang, D. (2003). Identification of Shp-2 as a Stat5A phosphatase. J. Biol. Chem. *278*, 16520–16527.

Chen, L., Sung, S.S., Yip, M.L., Lawrence, H.R., Ren, Y., Guida, W.C., Sebti, S.M., Lawrence, N.J., and Wu, J. (2006). Discovery of a novel shp2 protein tyrosine phosphatase inhibitor. Mol. Pharmacol. *70*, 562–570.

Danilova, N., and Gazda, H.T. (2015). Ribosomopathies: how a common root can cause a tree of pathologies. Dis. Model. Mech. *8*, 1013–1026.

DePristo, M.A., Banks, E., Poplin, R., Garimella, K.V., Maguire, J.R., Hartl, C., Philippakis, A.A., del Angel, G., Rivas, M.A., Hanna, M., et al. (2011). A framework for variation discovery and genotyping using next-generation DNA sequencing data. Nat. Genet. *43*, 491–498.

Doherty, L., Sheen, M.R., Vlachos, A., Choesmel, V., O'Donohue, M.F., Clinton, C., Schneider, H.E., Sieff, C.A., Newburger, P.E., Ball, S.E., et al. (2010). Ribosomal protein genes RPS10 and RPS26 are commonly mutated in Diamond-Blackfan anemia. Am. J. Hum. Genet. *86*, 222–228.

Elliott, S., Lorenzini, T., Chang, D., Barzilay, J., and Delorme, E. (1997). Mapping of the active site of recombinant human erythropoietin. Blood *89*, 493–502.

Flygare, J., Rayon Estrada, V., Shin, C., Gupta, S., and Lodish, H.F. (2011). HIF1alpha synergizes with glucocorticoids to promote BFU-E progenitor self-renewal. Blood *117*, 3435–3444.

Giani, F.C., Fiorini, C., Wakabayashi, A., Ludwig, L.S., Salem, R.M., Jobaliya, C.D., Regan, S.N., Ulirsch, J.C., Liang, G., Steinberg-Shemer, O., et al. (2016). Targeted Application of Human Genetic Variation Can Improve Red Blood Cell Production from Stem Cells. Cell Stem Cell *18*, 73–78.

Halupa, A., Bailey, M.L., Huang, K., Iscove, N.N., Levy, D.E., and Barber, D.L. (2005). A novel role for STAT1 in regulating murine erythropoiesis: deletion of STAT1 results in overall reduction of erythroid progenitors and alters their distribution. Blood *105*, 552–561.

Huang, L.J., Constantinescu, S.N., and Lodish, H.F. (2001). The N-terminal domain of Janus kinase 2 is required for Golgi processing and cell surface expression of erythropoietin receptor. Mol. Cell *8*, 1327–1338.

Jenni, S., Goyal, Y., von Grotthuss, M., Shvartsman, S.Y., and Klein, D.E. (2015). Structural Basis of Neurohormone Perception by the Receptor Tyrosine Kinase Torso. Mol. Cell *60*, 941–952.

Kenakin, T. (2011). Functional selectivity and biased receptor signaling. J. Pharmacol. Exp. Ther. *336*, 296–302.

Kenakin, T., Watson, C., Muniz-Medina, V., Christopoulos, A., and Novick, S. (2012). A simple method for quantifying functional selectivity and agonist bias. ACS Chem. Neurosci. *3*, 193–203.

Kirito, K., Uchida, M., Yamada, M., Miura, Y., and Komatsu, N. (1997). A distinct function of STAT proteins in erythropoietin signal transduction. J. Biol. Chem. *272*, 16507–16513.

Kirito, K., Nakajima, K., Watanabe, T., Uchida, M., Tanaka, M., Ozawa, K., and Komatsu, N. (2002). Identification of the human erythropoietin receptor region required for Stat1 and Stat3 activation. Blood *99*, 102–110.

Klein Herenbrink, C., Sykes, D.A., Donthamsetti, P., Canals, M., Coudrat, T., Shonberg, J., Scammells, P.J., Capuano, B., Sexton, P.M., Charlton, S.J., et al. (2016). The role of kinetic context in apparent biased agonism at GPCRs. Nat. Commun. *7*, 10842.

Knapp, D.J., Hammond, C.A., Aghaeepour, N., Miller, P.H., Pellacani, D., Beer, P.A., Sachs, K., Qiao, W., Wang, W., Humphries, R.K., et al. (2017). Distinct signaling programs control human hematopoietic stem cell survival and proliferation. Blood *129*, 307–318.

Kovacs, E., Zorn, J.A., Huang, Y., Barros, T., and Kuriyan, J. (2015). A structural perspective on the regulation of the epidermal growth factor receptor. Annu. Rev. Biochem. *84*, 739–764.

Kovanen, P.E., and Leonard, W.J. (2004). Cytokines and immunodeficiency diseases: critical roles of the gamma(c)-dependent cytokines interleukins 2, 4, 7, 9, 15, and 21, and their signaling pathways. Immunol. Rev. *202*, 67–83.

Krutzik, P.O., Trejo, A., Schulz, K.R., and Nolan, G.P. (2011). Phospho flow cytometry methods for the analysis of kinase signaling in cell lines and primary human blood samples. Methods Mol. Biol. *699*, 179–202.

Kuhrt, D., and Wojchowski, D.M. (2015). Emerging EPO and EPO receptor regulators and signal transducers. Blood *125*, 3536–3541.

Landowski, M., O'Donohue, M.F., Buros, C., Ghazvinian, R., Montel-Lehry, N., Vlachos, A., Sieff, C.A., Newburger, P.E., Niewiadomska, E., Matysiak, M., et al. (2013). Novel deletion of RPL15 identified by array-comparative genomic hybridization in Diamond-Blackfan anemia. Hum. Genet. *132*, 1265–1274.

Lek, M., Karczewski, K.J., Minikel, E.V., Samocha, K.E., Banks, E., Fennell, T., O'Donnell-Luria, A.H., Ware, J.S., Hill, A.J., Cummings, B.B., et al.; Exome Aggregation Consortium (2016). Analysis of protein-coding genetic variation in 60,706 humans. Nature *536*, 285–291.

Lemmon, M.A., and Schlessinger, J. (2010). Cell signaling by receptor tyrosine kinases. Cell *141*, 1117–1134.

Lemmon, M.A., Freed, D.M., Schlessinger, J., and Kiyatkin, A. (2016). The Dark Side of Cell Signaling: Positive Roles for Negative Regulators. Cell *164*, 1172–1184.

Liu, X., Jian, X., and Boerwinkle, E. (2011). dbNSFP: a lightweight database of human nonsynonymous SNPs and their functional predictions. Hum. Mutat. *32*, 894–899.

Ludwig, L.S., Gazda, H.T., Eng, J.C., Eichhorn, S.W., Thiru, P., Ghazvinian, R., George, T.I., Gotlib, J.R., Beggs, A.H., Sieff, C.A., et al. (2014). Altered translation of GATA1 in Diamond-Blackfan anemia. Nat. Med. *20*, 748–753.

MacArthur, D.G., Manolio, T.A., Dimmock, D.P., Rehm, H.L., Shendure, J., Abecasis, G.R., Adams, D.R., Altman, R.B., Antonarakis, S.E., Ashley, E.A., et al. (2014). Guidelines for investigating causality of sequence variants in human disease. Nature *508*, 469–476.

Manglik, A., Kim, T.H., Masureel, M., Altenbach, C., Yang, Z., Hilger, D., Lerch, M.T., Kobilka, T.S., Thian, F.S., Hubbell, W.L., et al. (2015). Structural Insights into the Dynamic Process of β2-Adrenergic Receptor Signaling. Cell *161*, 1101–1111.

McKeithan, T.W. (1995). Kinetic proofreading in T-cell receptor signal transduction. Proc. Natl. Acad. Sci. USA *92*, 5042–5046.

McLaren, W., Pritchard, B., Rios, D., Chen, Y., Flicek, P., and Cunningham, F. (2010). Deriving the consequences of genomic variants with the Ensembl API and SNP Effect Predictor. Bioinformatics *26*, 2069–2070.

Meyer, S.C., Keller, M.D., Chiu, S., Koppikar, P., Guryanova, O.A., Rapaport, F., Xu, K., Manova, K., Pankov, D., O'Reilly, R.J., et al. (2015). CHZ868, a Type II JAK2 Inhibitor, Reverses Type I JAK Inhibitor Persistence and Demonstrates Efficacy in Myeloproliferative Neoplasms. Cancer Cell *28*, 15–28.

Moraga, I., Richter, D., Wilmes, S., Winkelmann, H., Jude, K., Thomas, C., Suhoski, M.M., Engleman, E.G., Piehler, J., and Garcia, K.C. (2015a). Instructive

roles for cytokine-receptor binding parameters in determining signaling and functional potency. Sci. Signal. *8*, ra114.

Moraga, I., Wernig, G., Wilmes, S., Gryshkova, V., Richter, C.P., Hong, W.J., Sinha, R., Guo, F., Fabionar, H., Wehrman, T.S., et al. (2015b). Tuning cytokine receptor signaling by re-orienting dimer geometry with surrogate ligands. Cell *160*, 1196–1208.

Narla, A., Vlachos, A., and Nathan, D.G. (2011). Diamond Blackfan anemia treatment: past, present, and future. Semin. Hematol. *48*, 117–123.

Purcell, S., Neale, B., Todd-Brown, K., Thomas, L., Ferreira, M.A., Bender, D., Maller, J., Sklar, P., de Bakker, P.I., Daly, M.J., and Sham, P.C. (2007). PLINK: a tool set for whole-genome association and population-based linkage analyses. Am. J. Hum. Genet. *81*, 559–575.

Quintás-Cardama, A., Vaddi, K., Liu, P., Manshouri, T., Li, J., Scherle, P.A., Caulder, E., Wen, X., Li, Y., Waeltz, P., et al. (2010). Preclinical characterization of the selective JAK1/2 inhibitor INCB018424: therapeutic implications for the treatment of myeloproliferative neoplasms. Blood *115*, 3109–3117.

Rajagopal, S., Ahn, S., Rominger, D.H., Gowen-MacDonald, W., Lam, C.M., Dewire, S.M., Violin, J.D., and Lefkowitz, R.J. (2011). Quantifying ligand bias at seven-transmembrane receptors. Mol. Pharmacol. *80*, 367–377.

Roder, F., Wilmes, S., Richter, C.P., and Piehler, J. (2014). Rapid transfer of transmembrane proteins for single molecule dimerization assays in polymer-supported membranes. ACS Chem. Biol. *9*, 2479–2484.

Rothbauer, U., Zolghadr, K., Muyldermans, S., Schepers, A., Cardoso, M.C., and Leonhardt, H. (2008). A versatile nanotrap for biochemical and functional studies with fluorescent fusion proteins. Mol. Cell. Proteomics *7*, 282–289.

Roy, V., Pérez, W.S., Eapen, M., Marsh, J.C., Pasquini, M., Pasquini, R., Mustafa, M.M., and Bredeson, C.N.; Non-Malignant Marrow Disorders Working Committee of the International Bone Marrow Transplant Registry (2005). Bone marrow transplantation for diamond-blackfan anemia. Biol. Blood Marrow Transplant. *11*, 600–608.

Sander, J., Ester, M., Kriegel, H.P., and Xu, X.W. (1998). Density-based clustering in spatial databases: The algorithm GDBSCAN and its applications. Data Min. Knowl. Discov. *2*, 169–194.

Sankaran, V.G., and Agrawal, P.B. (2013). Stimulating erythropoiesis in neonates. Am. J. Hematol. *88*, 930–931.

Sankaran, V.G., Ghazvinian, R., Do, R., Thiru, P., Vergilio, J.A., Beggs, A.H., Sieff, C.A., Orkin, S.H., Nathan, D.G., Lander, E.S., and Gazda, H.T. (2012). Exome sequencing identifies GATA1 mutations resulting in Diamond-Blackfan anemia. J. Clin. Invest. *122*, 2439–2443.

Sankaran, V.G., Ulirsch, J.C., Tchaikovskii, V., Ludwig, L.S., Wakabayashi, A., Kadirvel, S., Lindsley, R.C., Bejar, R., Shi, J., Lovitch, S.B., et al. (2015). X-linked macrocytic dyserythropoietic anemia in females with an ALAS2 mutation. J. Clin. Invest. *125*, 1665–1669.

Sergé, A., Bertaux, N., Rigneault, H., and Marguet, D. (2008). Dynamic multiple-target tracing to probe spatiotemporal cartography of cell membranes. Nat. Methods *5*, 687–694.

Silvennoinen, O., and Hubbard, S.R. (2015). Molecular insights into regulation of JAK2 in myeloproliferative neoplasms. Blood *125*, 3388–3392.

Spangler, J.B., Moraga, I., Mendoza, J.L., and Garcia, K.C. (2015). Insights into cytokine-receptor interactions from cytokine engineering. Annu. Rev. Immunol. *33*, 139–167.

Syed, R.S., Reid, S.W., Li, C., Cheetham, J.C., Aoki, K.H., Liu, B., Zhan, H., Osslund, T.D., Chirino, A.J., Zhang, J., et al. (1998). Efficiency of signalling through cytokine receptors depends critically on receptor orientation. Nature *395*, 511–516.

Tarailo-Graovac, M., Shyr, C., Ross, C.J., Horvath, G.A., Salvarinova, R., Ye, X.C., Zhang, L.H., Bhavsar, A.P., Lee, J.J., Drögemöller, B.I., et al. (2016). Exome sequencing and the management of neurometabolic disorders. N. Engl. J. Med. *374*, 2246–2255.

Tefferi, A. (2012). JAK inhibitors for myeloproliferative neoplasms: clarifying facts from myths. Blood *119*, 2721–2730.

Thomas, C., Moraga, I., Levin, D., Krutzik, P.O., Podoplelova, Y., Trejo, A., Lee, C., Yarden, G., Vleck, S.E., Glenn, J.S., et al. (2011). Structural linkage between ligand discrimination and receptor activation by type I interferons. Cell *146*, 621–632.

Ulirsch, J.C., Nandakumar, S.K., Wang, L., Giani, F.C., Zhang, X., Rogov, P., Melnikov, A., McDonel, P., Do, R., Mikkelsen, T.S., and Sankaran, V.G. (2016). Systematic functional dissection of common genetic variation affecting red blood cell traits. Cell *165*, 1530–1545.

Vogelsang, J., Kasper, R., Steinhauer, C., Person, B., Heilemann, M., Sauer, M., and Tinnefeld, P. (2008). A reducing and oxidizing system minimizes photobleaching and blinking of fluorescent dyes. Angew. Chem. Int. Ed. Engl. *47*, 5465–5469.

Wen, D., Boissel, J.P., Showers, M., Ruch, B.C., and Bunn, H.F. (1994). Erythropoietin structure-function relationships. Identification of functionally important domains. J. Biol. Chem. *269*, 22839–22846.

Wilmes, S., Beutel, O., Li, Z., Francois-Newton, V., Richter, C.P., Janning, D., Kroll, C., Hanhart, P., Hötte, K., You, C., et al. (2015). Receptor dimerization dynamics as a regulatory valve for plasticity of type I interferon signaling. J. Cell Biol. *209*, 579–593.

Wisler, J.W., Xiao, K., Thomsen, A.R., and Lefkowitz, R.J. (2014). Recent developments in biased agonism. Curr. Opin. Cell Biol. *27*, 18–24.

Wu, T.R., Hong, Y.K., Wang, X.D., Ling, M.Y., Dragoi, A.M., Chung, A.S., Campbell, A.G., Han, Z.Y., Feng, G.S., and Chin, Y.E. (2002). SHP-2 is a dual-specificity phosphatase involved in Stat1 dephosphorylation at both tyrosine and serine residues in nuclei. J. Biol. Chem. *277*, 47572–47580.

Yin, J., Straight, P.D., McLoughlin, S.M., Zhou, Z., Lin, A.J., Golan, D.E., Kelleher, N.L., Kolter, R., and Walsh, C.T. (2005). Genetically encoded short peptide tag for versatile protein labeling by Sfp phosphopantetheinyl transferase. Proc. Natl. Acad. Sci. USA *102*, 15815–15820.

You, C., Richter, C.P., Löchte, S., Wilmes, S., and Piehler, J. (2014). Dynamic submicroscopic signaling zones revealed by pair correlation tracking and localization microscopy. Anal. Chem. *86*, 8593–8602.

Yu, C.L., Jin, Y.J., and Burakoff, S.J. (2000). Cytosolic tyrosine dephosphorylation of STAT5. Potential role of SHP-2 in STAT5 regulation. J. Biol. Chem. *275*, 599–604.

STAR★METHODS

KEY RESOURCES TABLE

REAGENT OR RESOURCE	SOURCE	IDENTIFIER
Antibodies		
Anti-Human CD235a-APC	eBioscience	Cat#: 17-9987-42; Clone: HIR2 (also GA-R2); RRID: AB_2043823
Anti-Human CD71-FITC	eBioscience	Cat#: 11-0719-42; Clone: OKT9; RRID: AB_1724093
CD11b-PE	eBioscience	Cat#: 12-0118-42; Clone: ICRF44; RRID: AB_2043799
CD41a-PE	eBioscience	Cat#: 12-0419-42; Clone: HIP8; RRID: AB_10870785
Propidium Iodide	eBioscience	Cat#: 00-6990-50
Alexa Fluor-647 Mouse Anti-phospho-STAT1 (pY701)	BD Bioscience	Cat#: 612597; RRID:AB_399880
Alexa Fluor-647 Mouse Anti-phospho-STAT3 (pY705)	BD Bioscience	Cat#: 557815; RRID:AB_647144
Alexa Fluor-647 Mouse Anti-phospho-STAT5 (pY694)	BD Bioscience	Cat#: 612599; RRID: AB_399882
Stat1 p84/p91	Santa Cruz Biotechnology	Cat#: sc-346; RRID:AB_632435
Purified Mouse Anti-Stat1 (pY701)	BD Transduction Laboratories	Cat#: 612232; Clone: 4a; RRID:AB_399555
Purified Mouse Anti-Stat3	BD Transduction Laboratories	Cat#: 610189; Clone: 84/Stat3; RRID:AB_397588
Purified Mouse Anti-Stat3 (pY705)	BD Transduction Laboratories	Cat#: 612356; Clone: 4/P-STAT3; RRID:AB_399645
Purified Mouse Anti-Stat5	BD Transduction Laboratories	Cat#: 610191; Clone: 89/Stat5; RRID:AB_397590
Phospho-Stat5 (Tyr694) Antibody	Cell Signaling Technology	Cat#: 9351S; RRID: AB_331593
GAPDH Antibody (6C5)	Santa Cruz Biotechnology	Cat#: sc-32233; RRID: AB_627679
Goat anti-mouse	Bio-Rad	Cat#: 1705047; RRID: AB_1125753
Goat anti-rabbit	Bio-Rad	Cat#: 1705046; RRID: AB_11125757
Chemicals, Peptides, and Recombinant Proteins		
Dulbecco's Modified Eagle Medium-High Glucose (DMEM)	GIBCO	Cat#: 11965-118
Iscove's Modified Dulbecco's Medium (IMDM)	GIBCO	Cat#: 12440-061
Fetal Bovine Serum (FBS)	Atlanta Biologicals	Cat#: S11150
Human Holo-Transferrin	Sigma Aldrich	Cat#: T0665-1G
Penicillin-Streptomycin	GIBCO	Cat#: 15140-122
Human Serum, Type AB	Atlanta Biologicals	Cat#: S40110
Human Plasma, Type AB	Blood bank at Boston Children's Hospital	N/A
Humulin R (insulin)	Lilly	NDC 0002-8215-01
Heparin	Hospira	NDC 00409-2720-01
Epogen (recombinant erythropoietin)	Amgen	NDC 55513-267-10
Recombinant human stem cell factor (SCF)	Peprotech	Cat#: 300-07
Recombinant human interleukin-3 (IL-3)	Peprotech	Cat#: 200-03
4x Laemmli Sample Buffer	Bio-Rad	Cat#: 161-0747
Opti-MEM	GIBCO	Cat#: 31985-062

(*Continued on next page*)

Continued

REAGENT OR RESOURCE	SOURCE	IDENTIFIER
FuGENE 6 Transfection Reagent	Promega	Cat#: E2691
Fixation Buffer	BD Bioscience	Cat#: 554655
Perm Buffer III	BD Bioscience	Cat#: 558050
May-Grünwald Stain	Sigma-Aldrich	Cat#: MG500
Giemsa Stain	Sigma-Aldrich	Cat#: GS500
Permount	Fisher Scientific	Cat#: SP15-500
Ruxolitinib (INCB018424)	Selleckchem	Cat#: S1378
NSC87877	Tocris	Cat#: 2613
CHZ868	MedKoo Biosciences	Cat#: 407137
Dimethyl sulfoxide (DMSO)	Sigma-Aldrich	Cat#: D2438
Critical Commercial Assays		
PrimityBio Pathway Phenotyping Service	Primity Bio	N/A
NucleoBond Xtra Maxi	Clontech	Cat#: 740414.50
MTT Cell Proliferation Assay	ATCC	Cat#: 30-1010k
4-20% Mini-PROTEAN TGX Precast Protein Gels, 15-well	Bio-Rad	Cat#: 4561096
Clarity Western ECL Substrate	Bio-Rad	Cat#: 170-5060
RIPA Lysis Buffer System	Santa Cruz Technology	Cat#: sc-24948A
Immobilon-P Membrane, PVDF	EMD Millipore	Cat#: IPVH00010
UltraComp eBeads	eBioscience	Cat#: 01-2222-42
RNeasy Mini Kit	QIAGEN	Cat#: 74104
iScript cDNA synthesis Kit	Bio-Rad	Cat#: 1708891
iQ SYBR Green Supermix	Bio-Rad	Cat#: 170-8882
PfuTurbo DNA Polymerase Alternative Detergent	Agilent	Cat#: 600255
Size Exclusion Chromatography Column, Superdex 200 Increase	GE Healthcare Life Sciences	Cat#: 28990944
Superdex 200 5/150GL Column	GE Healthcare Life Sciences	Cat#: 28906561
Series S Sensor Chip CM5	GE Healthcare Life Sciences	Cat#: BR100530
Deposited Data		
Whole-exome sequencing data	https://www.ncbi.nlm.nih.gov/gap	dbGaP: phs000474.v2.p1
Experimental Models: Cell Lines		
Human CD34+ hematopoietic stem and progenitor cells	Fred Hutchinson Cancer Research Center	N/A
UT7/EPO cells	Moraga et al., 2015b	N/A
Recombinant DNA		
Monomeric variant of eGFP-EPOR	Moraga et al., 2015b	N/A
Sequence-Based Reagents		
shRNA_STAT1_TRCN0000004265	Sigma-Aldrich	Sequence: CCGGCCCTGAAGTATCTGTATCCA ACTCGAGTTGGATACAGATACTTCAGGGTTTTT
shRNA_STAT3_TRCN0000020840 (Referred as shSTAT3-1 in the main text)	Sigma-Aldrich	Sequence: CCGGGCTGACCAACAATCCCAAGA ACTCGAGTTCTTGGGATTGTTGGTCAGCTTTTT
shRNA_STAT3_TRCN0000020843 (Referred as shSTAT3-2 in the main text)	Sigma-Aldrich	Sequence: CCGGGCAAAGAATCACATGCCACTT CTCGAGAAGTGGCATGTGATTCTTTGCTTTTT
STAT1 primer (forward)	Synthesized by Life Technologies	Sequence: CTAGTGGAGTGGAAGCGGAG
STAT1 primer (reverse)	Synthesized by Life Technologies	Sequence: CACCACAAACGAGCTCTGAA
STAT3 primer (forward)	Synthesized by Life Technologies	Sequence: GGAGGAGTTGCAGCAAAAAG
STAT3 primer (reverse)	Synthesized by Life Technologies	Sequence: TGTGTTTGTGCCCAGAATGT
STAT5 primer (forward)	Synthesized by Life Technologies	Sequence: AGATGCTGGCCGAGGTCAAC

(*Continued on next page*)

Continued

REAGENT OR RESOURCE	SOURCE	IDENTIFIER
STAT5 primer (reverse)	Synthesized by Life Technologies	Sequence: AGACTTGGCCTGCTGCTCAC
ACTB primer (forward)	Synthesized by Life Technologies	Sequence: AGAAAATCTGGCACCACACC
ACTB primer (reverse)	Synthesized by Life Technologies	Sequence: GGGGTGTTGAAGGTCTCAAA
Software and Algorithms		
ImageJ 1.50i	NIH	https://imagej.nih.gov/ij/
Microsoft Excel (2011)	Microsoft	https://products.office.com/en-us/excel
GraphPad Prism 7	GraphPad Software Inc	http://www.graphpad.com/scientific-software/prism/
FlowJo 10.0.8r1	FlowJo	https://www.flowjo.com/solutions/flowjo
R version 3.2	The R Foundation	https://www.r-project.org
Multiple-target tracing algorithm	Sergé et al., 2008 Wilmes et al., 2015	N/A
Density-based spatial clustering of applications with noise algorithm	Sander et al., 1998 Roder et al., 2014	N/A
GATK	DePristo et al., 2011	https://software.broadinstitute.org/gatk/
Plink	Purcell et al., 2007	https://www.cog-genomics.org/plink2
Picard tools	Broad Institute	https://broadinstitute.github.io/picard/
ExAC	Lek et al., 2016	http://exac.broadinstitute.org
Variant Effect Predictor v83	McLaren et al., 2010	www.ensembl.org/info/docs/tools/vep/
dbNSFP	Liu et al., 2011	https://sites.google.com/site/jpopgen/dbNSFP
Other		
BD Accuri C6	BD Biosciences	N/A
BD LSR Fortessa	BD Biosciences	N/A
Amersham Hyperfilm ECL	GE Healthcare Life Science	Cat#: 28906838
Shandon Cytospin 4	Thermo Electron Corporation	N/A
EnSpire Multimode Plate Reader	PerkinElmer	N/A
Dawn Heleos-II Multi-Angle Static Light Scattering	Wyatt Technology	N/A
Optilab T-rEX	Wyatt Technology	N/A
Biacore T200	GE Healthcare Life Sciences	Cat#: 28975001
T100 Thermal Cycler	Bio-Rad	N/A
CFX96 Real-Time System	Bio-Rad	N/A
IX71	Olympus	N/A
iXon DU897D, 512x512 pixel	Ando Technology	N/A
UAPO 150x/ 1.45 TIRFM	Olympus	N/A
DualView	Optical Insight	N/A
640 DCXR dichroic beam splitter	Chroma	N/A
Bandpass filter 585/40	Semrock	N/A
Bandpass filter 690/70	Chroma	N/A
Z2 Coulter Counter	Beckman Coulter	N/A

CONTACT FOR REAGENT AND RESOURCE SHARING

Requests for further information or reagents may be directed to the Lead Contact, Vijay G. Sankaran (sankaran@broadinstitute.org).

EXPERIMENTAL MODEL AND SUBJECT DETAILS

UT7/EPO Cell Culture

UT7/EPO cells were maintained in Dulbecco's Modified Eagle Medium (DMEM; GIBCO) with 10% of fetal bovine serum (FBS; Atlanta Biologicals), 1% of penicillin/ streptomycin (GIBCO), and 2 U/mL recombinant erythropoietin (EPO) (Amgen) (Moraga et al., 2015b). The culture was passaged every 2-3 days. Cells were incubated at 37°C with 20% O_2 and 5% CO_2.

Primary Cell Culture

$CD34^+$ hematopoietic stem and progenitor cells from mobilized peripheral blood were purchased from the Fred Hutchinson Cancer Research Center. $CD34^+$ cells were cultured via a previously described culture system that allows complete maturation into enucleated red blood cells (Giani et al., 2016; Ludwig et al., 2014). The base media for erythroid differentiation was composed of 2% human AB plasma (obtained from the blood bank at Boston Children's Hospital), 3% human AB serum (Atlanta Biologicals), 1% of penicillin/streptomycin, 3 U/mL heparin (Hospira), 10 μg/mL insulin (Lilly), 200 μg/mL transferrin (Sigma) in Iscove's Modified Dulbecco's Medium (IMDM; GIBCO). In Phase I (day 0-6), cultures were supplemented with 10 ng/mL stem cell factor (SCF), 1 ng/mL interleukin-3 (IL-3), and either with recombinant EPO from Amgen (3 U/mL), EPO WT (10^{-9} M) or EPO R150Q (10^{-9} or 10^{-7} M) to initiate erythroid lineage commitment. In Phase II (day 7-13) and Phase III (day 14 onward), cultures were supplemented with SCF and EPO (either with WT or R150Q) or EPO alone, respectively, to promote further erythroid differentiation. Cells were incubated at 37°C with 20% O_2 and 5% CO_2. Cell concentration was measured using an automatic cell counter (Beckman Coulter).

METHOD DETAILS

Recombinant Protein Expression and Purification

Codon-optimized cDNAs for the extracellular region of human erythropoietin receptor (EPOR) and human erythropoietin (EPO) were synthesized (Genscript). The sequence was subcloned into a pFastbac plasmid for baculovirus driven expression in insect cells. The mature protein sequence followed the native signal peptide of each. A hexa-histidine tag was added to the amino terminus, following 193R of EPO, and following 249D of EPOR. Mutation of arginine 177 to glutamine – residue 150 of the mature EPO sequence after signal sequence processing and referred to as (EPO R150Q) – was introduced by site directed mutagenesis using the QuickChange Kit (Agilent Technologies). The EPO site II mutation of serine 127 to glutamic acid – residue 100 of the mature EPO sequence (S100E) – was introduced by site directed mutagenesis using the QuickChange Kit (Agilent Technologies).

EPO, EPO mutants, and the EPOR were expressed and purified as described (Jenni et al., 2015). *Trichoplusia ni* cells were grown in Ex-Cell405 (Sigma-Aldrich) medium and infected at 1 million/ml. Supernatant was clarified 72 hr post infection by centrifugation and passed twice over cobalt resin (Clontech). For EPOR, protease inhibitors were added to the supernatant (aprotinin, leupeptin, and pepstatin). The resin was washed with 10 mM imidazole in Dulbecco's modified phosphate-buffered saline (Sigma-Aldrich) and eluted in the same buffer with 200 mM imidazole. After adding 10 mM ethylenediaminetetraacetic acid (EDTA) the protein was concentrated in a Centricon 10 kDa spin concentrator (Millipore) and then passed over a Superdex 200 10/300 GL size exclusion chromatography column (GE Healthcare Life Sciences) in 10 mM triethanolamine buffer (pH 8.0), with 150 mM NaCl.

Mass Spectrometry

Protein identity and purity were assessed by intact protein electrospray ionization fourier transform ion cyclotron resonance mass spectrometry (ESI-FTICR MS; Bruker Apex 3) after desalting samples by reversed-phase liquid chromatography (RPLC). Both WT and mutant R150Q EPO ran as single peaks on RPLC. The mass spectra of both proteins showed the same pattern of glycosylation, with the deconvoluted masses of all 9 major glycosylated species of the mutant shifted shifted 28 amu lower, consistent with the R150Q mutation.

Microcapillary LC/MS/MS of Coomassie stained bands digested with trypsin matched peptides corresponding to > 81% of human EPO. For the WT EPO sample the fragment 144-VYSNFLR-150 was isolated, whereas 144-VYSNFLQGK-152 was isolated for the R150Q mutant. The remaining unmatched peptide fragments include the predicted glycosylation sites.

Surface Plasmon Resonance

Using a Biacore T200 instrument (GE Life Sciences) EPOR was coupled to a series S CM5 chip (GE Life Sciences) after dilution to ~500 nM in 10 mM acetate pH 5.2 buffer. A total of 700 response units (RUs) were stably coupled. 10 mM triethanolamine buffer (pH 8.0), with 100 mM NaCl was used as running buffer for equilibrium experiments. 150 μL of EPO or EPO R150Q was injected at various concentrations with a flow rate of 30 μl/min all at 8°C. A regeneration step of 25 μL of 10 mM acetate pH 5.0, 1 M NaCl between injections at a rate of 50 μl/min returned the baseline to $\leq$ 5% of the initial RUs. Equilibrium (plateau) RUs were plotted against concentration and a non-linear regression analysis was carried out to determine dissociation constants (GraphPad Prism 6.0). The fit included a shared Bmax between wild-type and mutant, as each should give the same potential max response to the equivalent surface. Four separate experiments were combined to calculate the average and error. For kinetic experiments with the site II mutant (S100E) EPO ligands, the buffer included 0.05% Tween 20 (Polyethylene glycol sorbitan monolaurate). Maximum RUs were kept less than 100. 250 μL of EPO or EPO R150Q was injected in at various concentrations with a flow rate of 50 μl/min all at 15°C. A regeneration step of 25 μL of 10 mM acetate pH 5.0, 1 M NaCl between injections at a rate of 50 μl/min returned the baseline to $\leq$ 5% of the initial RUs. Fitting was carried out with Biacore evaluation software.

Size Exclusion Chromatography-Multiangle Light Scattering (SEC-MALS)

This was performed essentially as described (Jenni et al., 2015). SEC-MALS was carried out on a Dawn Heleos-II Multi-Angle static Light Scattering (MALS) detector (Wyatt) with the Optilab T-Rex refractive index detector (Agilent Technologies) after passing through

a Superdex 200 5/150 GL column (GE Healthcare Life Sciences). A total of 15 μL of 40 μM EPO, EPO R150Q, or 38 μM EPO receptor extracellular region (EPOR) was injected. For the 1:1 ratios (Ligand: EPOR), 29 μM: 29 μM was injected. Fitting was done with Astra software using a dn/dc value of 0.179, which assumes 14% carbohydrate by mass for each protein.

Proliferation Assay

UT7/EPO cells were cytokine starved overnight before plating. 5,000 or 10,000 cells were plated in 96-well plates (Corning) with the various recombinant EPO ligands (WT, R150Q, S100E, and R150Q+S100E) at a range of concentrations (0, 10^{-14}-10^{-6} M). For inhibitor experiments, UT7/EPO cells were cytokine starved as above and treated with vehicle (water or DMSO), NSC87877 (Tocris), ruxolitinib (Selleckchem), or CHZ868 (MedKoo) at a range of concentrations (0, $4x10^{-10}$-$5x10^{-6}$ M). The cytokine starved UT7/EPO cells were treated with vehicle (DMSO) or S3I-201 (Selleckchem) ($75x10^{-6}$ - $500x10^{-6}$ M). Cells were also treated with 40 nM of ruxolitinib with the recombinant EPO ligands (WT, R150Q) at a range of concentrations (0, 10^{-12}-10^{-6} M). Cells were incubated at 37°C with 20% O_2 and 5% CO_2 for 3 days before performing the MTT assay (ATCC) to assess proliferation. This was done following the manufacturer's protocol. Briefly, tetrazolium MTT (3-(4,5-dimethylthiazolyl-2)-2,5-diphenyltetrazolium bromide) was added to cells and incubated at 37°C for 3 hr. Subsequently, the detergent reagent was added and incubated at room temperature in the dark for 3 hr. The level of intracellular formazan resulting from cell proliferation was measured via absorbance at 570 nm using the EnSpire Multimode Plate Reader (PerkinElmer). To calculate the relative proliferation, the absorbance of blank wells (media only) and of wells containing unstimulated cells was subtracted from the absorbance for the other wells. The relative proliferation was calculated by normalizing all readings to the absorbance value of WT EPO at 10^{-9} M.

Evaluation of Erythroid Maturation

To monitor the stages of erythroid maturation, Giemsa staining was performed. Differentiated cells were spun down using Shandon Cytospin (Thermo Electron Corporation) at 400 rpm for 3 min. Slides (Sigma) with cytocentifuged cells were stained with May-Grünwald (Sigma) for 5 min at room temperature. After washing three times with deionized water for 30 s each, slides were stained with a 1:20 dilution of Giemsa (Sigma) for 15 min at room temperature. Slides were washed three times with deionized water followed by air drying, before mounting a coverslip (Thermo Scientific) with permount (Sigma). Each stage of erythroid maturation was manually counted after evaluating at least five different fields of a slide. Images were taken at 100x via on an Olympus BX51 microscope.

Flow Cytometry

Hematopoietic differentiation under treatment with EPO WT or EPO R150Q was evaluated and compared by flow cytometry. Cells were washed with a buffer containing 3% FBS in PBS, followed by staining with antibodies at 4°C in the dark for 20 min. Differentiated cells were stained with CD71-Fluorescein Isothiocyanate (FITC) and CD235a-Allophycocyanin (APC) for erythroid cell evaluation or CD11b/ CD41a-Phycoerythrin (PE) for non-erythroid myeloid cell evaluation. Propidium Iodide (PI; 1:1,000 dilution) was added for live/dead cell discrimination. All antibodies were stained at a 1:40 dilution, unless otherwise noted. A BD Accuri C6 Cytometer (BD Bioscience) was used to acquire flow cytometry data and all analysis was performed using FlowJo (version 10.0.8r1).

Phosphorylated STAT Assessment with Intracellular Flow Cytometry

Cytokine starved UT7/EPO cells were treated in a dose-dependent (0, 10^{-12}-10^{-6} M of EPO WT or R150Q for 30 min) or time-dependent (10^{-9} or 10^{-7} M of EPO WT or R150Q, respectively, for 15, 30, 60, and 180 min) manner. Starvation took place in base media without EPO present. UT7/EPO cells were generally starved overnight. When necessary, cytokine starved UT7/EPO cells were pretreated with inhibitors for 30 min in a dose-dependent (0, $5x10^{-10}$-$5x10^{-5}$ M of NSC87877, ruxolitinib, or CHZ868) followed by stimulation with EPO in the presence of inhibitors. For primary human erythroid cell cultures, $CD34^+$ HSPCs were differentiated toward the erythroid lineage for 8 days followed by 4 hr of starvation in 1% bovine serum albumin (BSA) in IMDM. Subsequently, starved cells were stimulated with EPO (WT or R150Q) for 1 hr. Treated cells were gently mixed with pre-warmed Fixation Buffer (BD Bioscience) at 37°C for 10 min to fix cells. To permeabilize cells for intracellular staining, cells were resuspended in pre-chilled Perm Buffer III (BD Bioscience) for 30 min at 4°C. After three washes with 3% FBS in PBS, samples were stained either with Alexa Fluor-647 Mouse Anti-phospho-STAT5 (pY694; 1:20 dilution), Alexa Fluor-647 Mouse Anti-phospho-STAT3 (pY705; 1:20 dilution), or Alexa Fluor-647 Mouse Anti-phospho-STAT1 (pY701; 1:20 dilution) for 1 hr in the dark at room temperature. A BD Accuri C6 Cytometer (BD Bioscience) was used to acquire mean fluorescent intensity (MFI) of phospho-STAT1/3/5-Alexa Fluor 647. The MFI of phospho-STAT1/3/5-Alexa Fluor 647 of gated single cells was calculated using FlowJo (version 10.0.8r1). Unstimulated UT7/EPO cells were used as a negative control. For pSTAT5 analysis in primary human erythroid cells, we gated on pSTAT5-positive cells for the analysis due to the heterogeneity of EPO response in such primary cell cultures. Data were acquired using either Accuri or LSR Fortessa instruments (Becton, Dickinson and Company).

Western Blotting

The cytokine starved UT7/EPO cells were stimulated with the recombinant EPO ligands (WT and R150Q) at a range of concentrations (0, 10^{-12}-10^{-6}M) for 30 min. Cells were collected and washed twice with cold PBS before lysing cells. Cells were lysed with RIPA

buffer (Santa Cruz Technology) supplemented with PMSF, protease inhibitor cocktail, sodium orthovanadate, sodium pyrophosphate, beta-glycerol phosphate, and sodium fluoride. The protein lysates were added with loading dye and beta-mercaptoethanol and boiled at 95°C for 5 min. Equal amount of proteins (6.7 μg for STAT1, pSTAT1, STAT3, and pSTAT3; 1.7 μg for STAT5 and pSTAT5) were loaded for all conditions into 4%–20% Mini-PROTEAN TGX Precase Protein Gels for protein electrophoresis. Precision Plus Protein Kaleidoscope Prestained Standards (Bio-Rad) were used as a ladder to determine the molecular weight of proteins. Once the protein electrophoresis is completed, proteins were transferred to equilibrated PVDF membrane in 1x Tri/Glycine with 10% MeOH at 4C for 90 min. Then, the membrane was blocked with 3% BSA in TBS-T buffer for 1 hr at room temperature followed by incubation with the primary antibodies overnight at 4°C. Then, HRP conjugated secondary antibodies were incubated at 1 hr at room temperature. The membranes were developed by the incubation with substrates of the Clarity Western ECL Substrate (Bio-Rad) for 5 min prior to developing into films. Films were scanned and bands were quantified using ImageJ 1.50i. The following primary antibody dilutions were used in the study: STAT1 (Santa Cruz Biotechnology; 1:200), pSTAT1 (BD Transduction Laboratories; 1:1,000), STAT3 (BD Transduction Laboratories; 1:5,000), pSTAT3 (BD Transduction Laboratories; 1:5,00), STAT5 (BD Transduction Laboratories; 1:500), pSTAT5 (Cell Signaling Technology; 1:2,000), and GAPDH (Santa Cruz Technology; 1:5,000). For secondary antibodies, goat anti-rabbit (Bio-Rad) was used in 1:20,000 and goat anti-mouse (Bio-Rad) was used in 1:10,000.

Phosphorylated Protein Analysis

Cytokine starved UT7/EPO cells were treated with EPO WT (10^{-9} M) or EPO R150Q (10^{-7} M) for 15 and 30 min after overnight starvation. Cells were fixed with 8% paraformaldehyde in PBS for 10 min at room temperature. Then, samples were resuspended in 5% bovine serum albumin in PBS and were stored at −80°C. The fixed cells were prepared for antibody staining according to standard protocols (Krutzik et al., 2011). Briefly, the fixed cells were permeabilized in 90% methanol for 15 min. The cells were stained with a panel of antibodies specific to the markers indicated (Primity Bio Pathway Phenotyping service, Table S5) and analyzed on an LSRII flow cytometer (Becton Dickinson). The mean fluorescence intensities (MFI) of the stimulated samples and unstimulated control samples were calculated. Ratios of the individual MFIs (using unstimulated as a reference) and of the distribution of MFIs at the different time points were analyzed using R 3.2 (R-project).

Viral Production and Infection

293T cells were cultured in DMEM with 10% FBS and 1% P/S. Cells were passaged with 0.25% Trypsin when they reached 80% confluency. A day before transfection, 293T cells were cultured with DMEM with 10% FBS in the absence of antibiotics. Cells were co-transfected with pVSVG, pΔ8.9, and a lentiviral genomic plasmid of interest (shLuc, shRNA targeting STAT1: TRCN0000004265, shRNA targeting STAT1: TRCN0000004267, shRNA targeting STAT3: TRCN0000020840, or shRNA targeting STAT3: TRCN0000020843). Media was replenished the day after transfection, and the supernatant containing virus was collected approximately 48 hr post-transfection. Collected supernatant was filtered through a 0.45 μm filter to proceed with viral infection. Approximately 300,000-500,000 UT7/EPO cells or $CD34^+$ cells (day 2 in culture) were infected with the prepared lentivirus along with polybrene (8 μg/mL) and recombinant EPO (for UT7/EPO) or recombinant EPO/ SCF/ IL-3 (for $CD34^+$ cells). Cells with viral supernatant were spun down at 2000 RPM for 90 min and were incubated at 37°C overnight. Virus was washed a day after infection, and puromycin selection (2 μg/mL for UT7/EPO cells and 1 μg/mL for HSPCs) was initiated on the following day for 30 hr. Puromycin-selected UT7/EPO cells were plated for proliferation assays for 2 days, as described above. Cell concentrations after puromycin-selection of HSPC cell cultures were measured using an automated cell counter and growth was tracked on subsequent days of the erythroid differentiation culture (Beckman Coulter).

RNA Extraction, cDNA Synthesis, and Quantitative RT-PCR

UT7/EPO cells with lentiviral infection were collected after puromycin selection. Cells were spun down at 600 g x 5 min at room temperature, and RNA was extracted with RNeasy Mini Kit following the manufacture's protocol (QIAGEN). Approximately 280 ng of RNA was used to synthesize cDNA with the iScript cDNA Synthesis Kit (Bio-Rad). Each reaction was incubated 5 min at 25°C for priming, 30 min at 46°C for reverse transcription, and additional 5 min at 95°C to inactivate the reverse transcriptase. Then, diluted cDNA (1:25) was mixed with iQ SYBR Green Supermix (Bio-Rad), 4 μM of primers listed above, and water to amplify using CFX 96 Read Time System (Bio-Rad) for 40 cycles. Samples without reverse transcriptase was used as negative controls for quantitative PCR reactions.

Single-Molecule Tracking, Co-localization, and Co-tracking Analyses

Overview

Single-molecule TIRF microscopy, labeling procedures, and co-localization/ co-tracking analyses were conducted as recently described (Moraga et al., 2015b). Single-molecule localization and single-molecule tracking were carried out using the multiple-target tracing (MTT) algorithm (Sergé et al., 2008), as described previously (You et al., 2014). Immobile molecules were identified by the density-based spatial clustering of applications with noise (DBSCAN) (Sander et al., 1998) algorithm, as described recently (Roder et al., 2014). For co-tracking analysis, immobile particles were excluded from the dataset. Individual molecules detected

in the both spectral channels were regarded as co-localized if a particle was detected in both channels of a single frame within a distance threshold of a 100 nm radius. The population of co-localized particles was linked frame-by-frame to co-trajectories (threshold: $\geq$ 10 consecutive steps).

Plasmid Constructs

For single molecule fluorescence microscopy, monomeric non-fluorescent (Y67F) variant of eGFP ("mXFP") was N-terminally fused to EPOR. This construct was inserted into a modified version of pSems-26 m (Covalys) including a signal peptide of Igκ. The ORF was linked to a neomycin resistance cassette via an IRES site. The construct JAK2-meGFP was co-expressed to ensure full functionality of the receptor system. For negative controls, we used a fusion construct of meGFP linked to an artificial transmembrane domain $K(ALA)_7KSSR$.

Cultivation of Cells for Single-Molecule Imaging

HeLa cells were cultivated at 37°C and 5% CO_2 in Minimal Essential Medium with Earle's Salts (EMEM) with stable glutamine supplemented with 10% fetal bovine serum (FBS), non-essential amino acids and HEPES buffer without addition of antibiotics. HeLa cells were stably transfected with mXFP-EPOR by selection with G418 (800μg/ml). For minimizing the background fluorescence from non-specifically adsorbed dye molecules in single molecule imaging experiments, glass coverslides were coated with a poly-L-lysine-graft-(polyethylene glycol) copolymer functionalized with RGD as described previously (You et al., 2014). Cells were seeded in 60 mm cell-culture dishes to a density of approximately 60% confluence and transiently transfected with JAK2-meGFP via calcium-phosphate-precipitation according to standard protocols. Transfected cells were transferred to coated 35 mm glass coverslides. Single molecule imaging experiments were conducted 48 hr post transfection. Imaging was performed in custom-designed microscopy chambers with a volume of 1 ml.

Protein Purification & Labeling

An anti-GFP nanobody (antiGFP-NB) (Rothbauer et al., 2008) fused to a C-terminal ybbR-tag (Yin et al., 2005) for site-specific labeling by enzymatic phosphopantetheinyl-transfer was cloned into the pBAC vector. Generation of a baculovirus and protein expression in *Sf*9 cells were carried out as described above. The protein was purified to homogeneity by immobilized metal ion affinity chromatography and labeled using coenzyme A conjugated to DY 647 and ATTO Rho11, respectively, according to published protocols (Yin et al., 2005). A typical labeling degree of > 90% was achieved.

Single Molecule Imaging Experiments

Single molecule imaging experiments were carried out by total internal reflection fluorescence (TIRF) microscopy with an inverted microscope (Olympus IX71) equipped with a triple-line total internal reflection (TIR) illumination condenser (Olympus) and a back-illuminated electron multiplied (EM) CCD camera (iXon DU897D, 512 × 512 pixel, Andor Technology). A 150 × magnification objective with a numerical aperture of 1.45 (UAPO 150 × /1.45 TIRFM, Olympus) was used for TIR illumination of the sample. All experiments were carried out at room temperature in medium without phenol red supplemented with an oxygen scavenger and a redox-active photoprotectant to minimize photobleaching (Vogelsang et al., 2008). For cell surface labeling of mXFP-EPOR, ^{DY647}antiGFP-NB and ^{RHO11}antiGFP-NB were added to the medium at equal concentrations (2 nM) and incubated for at least 5 min. The nanobodies were kept in the bulk solution during the whole experiment in order to ensure high equilibrium binding to mXFP-EPOR (Moraga et al., 2015b). Dimerization of EpoR was probed before and after incubation with indicated EPO mutants and concentrations. Model transmembrane protein, comprised of a N-terminal meGFP-tag, linked to an artificial transmembrane domain $(ALA)_7KSSR$ was labeled as described above and taken as negative control for co-tracking experiments.

Image stacks of 150 frames were recorded at 32 ms/frame. For simultaneous dual-color acquisition, ^{RHO11}antiGFP-NB was excited by a 561 nm diode-pumped solid-state laser at 0.95 mW ($\sim$32W/cm^2) and ^{DY647}antiGFP-NB by a 642 nm laser diode at 0.65 mW ($\sim$22W/cm^2). Fluorescence was detected using an spectral image splitter (DualView, Optical Insight) with a 640 DCXR dichroic beam splitter (Chroma) in combination with the bandpass filter 585/40 (Semrock) for detection of RHO11 and 690/70 (Chroma) for detection of DY647 dividing each emission channel into 512x256 pixel.

QUANTIFICATION AND STATISTICAL ANALYSIS

Single Molecule Tracking, Co-Localization and Co-Tracking Analyses

Single molecule localization and single molecule tracking were carried out using the multiple-target tracing (MTT) algorithm (Sergé et al., 2008), as described previously (Wilmes et al., 2015). Immobile molecules were identified by the density-based spatial clustering of applications with noise (DBSCAN) (Sander et al., 1998) algorithm as described recently (Roder et al., 2014). For co-tracking analysis, immobile particles were excluded from the dataset.

Prior to co-localization analysis, imaging channels were aligned with sub-pixel precision by using a spatial transformation. To this end, a transformation matrix was calculated based on a calibration measurement with multicolor fluorescent beads (TetraSpeck microspheres 0.1 μm, Invitrogen) visible in both spectral channels (cp2tform of type 'affine', The MathWorks MATLAB 2009a).

Individual molecules detected in the both spectral channels were regarded as co-localized, if a particle was detected in both channels of a single frame within a distance threshold of a 100 nm radius. For single molecule co-tracking analysis, the MTT algorithm was applied to this dataset of co-localized molecules to reconstruct co-locomotion trajectories (co-trajectories) from the identified population of co-localizations. For the co-tracking analysis, only trajectories with a minimum of 10 steps ($\sim$300 ms) were considered. The

relative fraction of co-tracked molecules was determined with respect to the absolute number of trajectories and corrected for EPOR stochastically double-labeled with the same fluorophore species as follows:

$$\text{rel. co-tracking} = \frac{AB}{2 \times \left[\left(\frac{A}{A+B}\right) \times \left(\frac{B}{A+B}\right)\right]}$$

where A, B, and AB are the numbers of trajectories observed for RHO11, DY647 and co-trajectories, respectively.

Statistical Analysis of Binding and Kinetic Data

The data points were fitted using the binding–saturation curve sigmoidal fits with the one site–total method (GraphPad Prism 7). The significance was calculated with a two sided Student's t test.

Whole-Exome Sequencing Analysis

The patient described here is part of a DBA cohort that underwent whole exome sequencing (raw sequence data has been deposited under dbGAP accession phs000474.v2.p1) (Doherty et al., 2010; Sankaran et al., 2012). Coverage across the consensus coding DNA sequences (CDS; downloaded from UCSC genome browser on December 13, 2015) plus an additional 20 nucleotides on each side of the exons was calculated using Picard tools (Table S1). The variant call file (VCF) was annotated with Variant Effect Predictor v83 and the dbNSFP database v3.1 (Liu et al., 2011; McLaren et al., 2010). A combination of the genome analysis toolkit (GATK) and Plink were then used to identify rare (based upon the ExAC v0.3 release of 60,706 individuals) variants (DePristo et al., 2011; Purcell et al., 2007). No rare (defined as 0.01% allele frequency in ExAC) damaging (missense or loss of function) mutations were present in the patient in any of the known DBA genes (*RPS19*, *RPL5*, *RPL11*, *RPL35A*, *RPS26*, *RPS24*, *RPS17*, *RPS7*, *RPS10*, *RPL26*, *RPS29*, *RPS28, RPS27, RPL27, RPL15*, *RPL31*, *GATA1*, *TSR2*), or in any other ribosome protein coding genes. Since the proband is the child of consanguineous parents, we next searched for putative recessive mutations in the known red cell disorder genes (*ANK1*, *SPTB*, *SPTA1*, *SLC4A1*, *EPB42*, *EPB41*, *PIEZO1*, *KCNN4*, *GLUT1*, *G6PD*, *PKLR*, *NT5C3A*, *HK1*, *GPI*, *PGK1*, *ALDOA*, *TPI1*, *PFKM*, *ALAS2*, *FECH*, *UROS*, *CDAN1*, *SEC23B*, *KIF23*, *KLF1*, *GATA1*, *HBB*, *HBA1*, *HBA2*), but again did not identify any rare damaging mutations. Having ruled out previously identified causal genes, we expanded our search space to all putative rare and damaging recessive mutations (Table S2) and identified chr7:100320704:G>A in the *EPO* gene as the leading candidate mutation (Table S3). Follow-up Sanger sequencing confirmed the mutation and showed that this mutation showed appropriate segregation in the family, consistent with a model of complete penetrance.

Cell

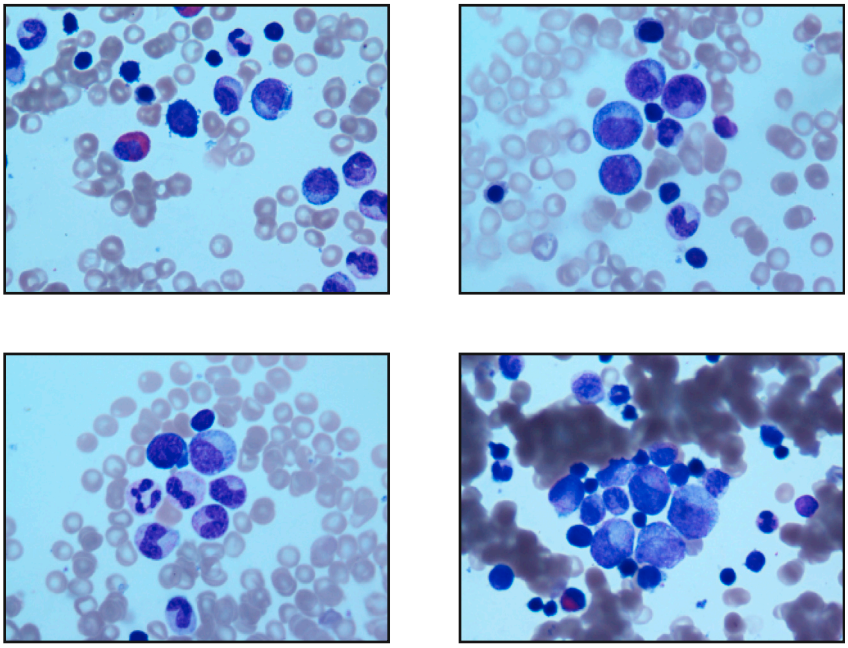

Figure S1. Bone Marrow Aspirate Images from Patient, Related to Figure 1

Bone marrow aspirate images taken at 100× magnification from the proband. The paucity of erythroid precursors with identifiable cells from other lineages are depicted.

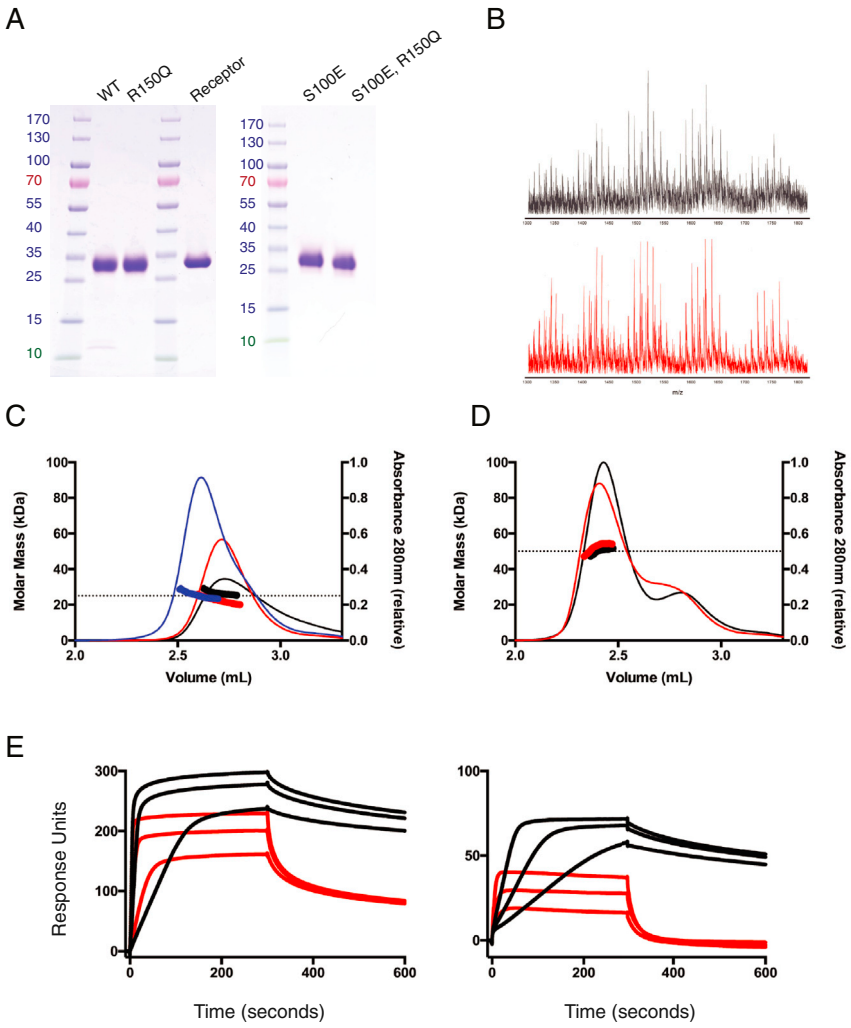

Figure S2. EPO Complex Formation with the EPO Receptor, Related to Figure 2

(A) A reducing SDS Coomassie gel of purified proteins, 2.3 μg of each: EPO (WT), EPO mutant (R150Q), and the EPO receptor extracellular region (Receptor). On a second gel 3.2 μg of each site 2 mutant: EPO S100E and the double mutant S100E+R150Q.

(B) Electrospray mass spectra traces of EPO WT (black) and R150Q (red) showing the same pattern of glycosylation, with the deconvoluted masses of all nine major glycosylated species of the mutant shifted shifted 28 amu lower, consistent with the R150Q mutation.

(C) SEC-MALS of monomeric proteins, 15 μL of 40 μM each: Wild-type EPO (black), EPO R150Q (red) and the EPO receptor (blue). The determined mass is shown as a colored heavy line. The dashed line indicates the approximate expected weight of the monomeric components ~25 kDa.

(D) SEC-MALS of 1:1 complexes, 15 μL of 29 μM each: Wild-type EPO plus EPO receptor (black); and EPO R150Q plus EPO receptor (red). The determined mass is shown as a colored heavy line. The dashed line indicates the expected mass of the 1:1 complex between EPO and its receptor.

(E) Representative sensograms from surface plasmon resonance experiments. The wild-type (black) or R150Q mutant (red) are shown in the unmutated (left) or S100E (right) background. The traces are shown at ligand concentrations of 250, 125 and 62.5 nM for both wild-type and R150Q in the unmutated background (left), while they are shown for 50, 25, and 12.5 nM for the wild-type and 62.5, 31.3, and 15.6 nM for the R150Q in the S100E background (right).

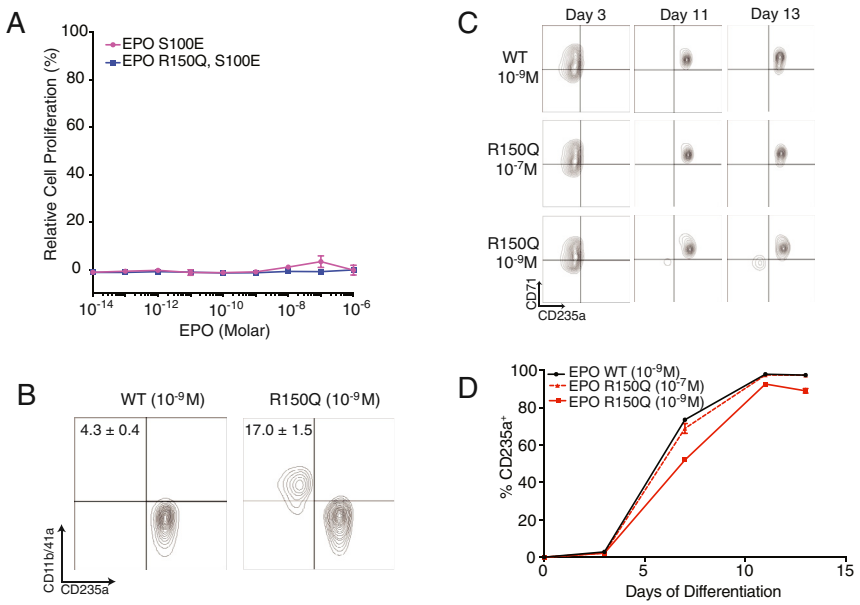

Figure S3. Analysis of Cellular Phenotypes of the EPO R150Q Mutant, Related to Figure 3

(A) Proliferation of UT7 cells stimulated with EPO ligands containing S100E (site 2) mutation. The results are shown as the mean ± SEM of the mean from two independent experiments.

(B) Myeloid cells as assessed on day 13 using the surface markers CD11b and CD41a, while erythroid cells are assessed with CD235a. The percentage of myeloid cells is plotted in the top left corner as the mean ± SEM from three independent experiments.

(C) Erythroid differentiation as assessed using flow cytometry during the differentiation cultures of primary human hematopoietic stem and progenitor cells are shown from various days. The plots are representative of three independent experiments.

(D) Percentage of cells expressing CD235a at different time points during erythroid differentiation in vitro. The results are shown as the mean ± SEM from three independent experiments.

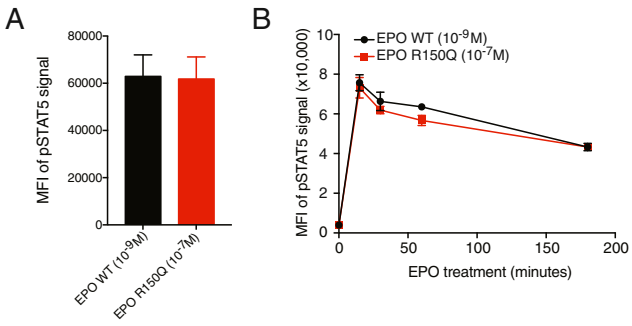

Figure S4. Similar STAT5 Phosphorylation by EPO WT or R150Q, Related to Figure 4

(A) The absolute value of MFI of pSTAT5 at maximal potency of EPO WT (10^{-9}M) and R150Q (10^{-7}M) are shown. The results are shown as the mean ± SEM of the mean from 3 independent experiments.

(B) Time dependent absolute value of MFI of pSTAT5. Means ± SEM for two independent experiments are shown.

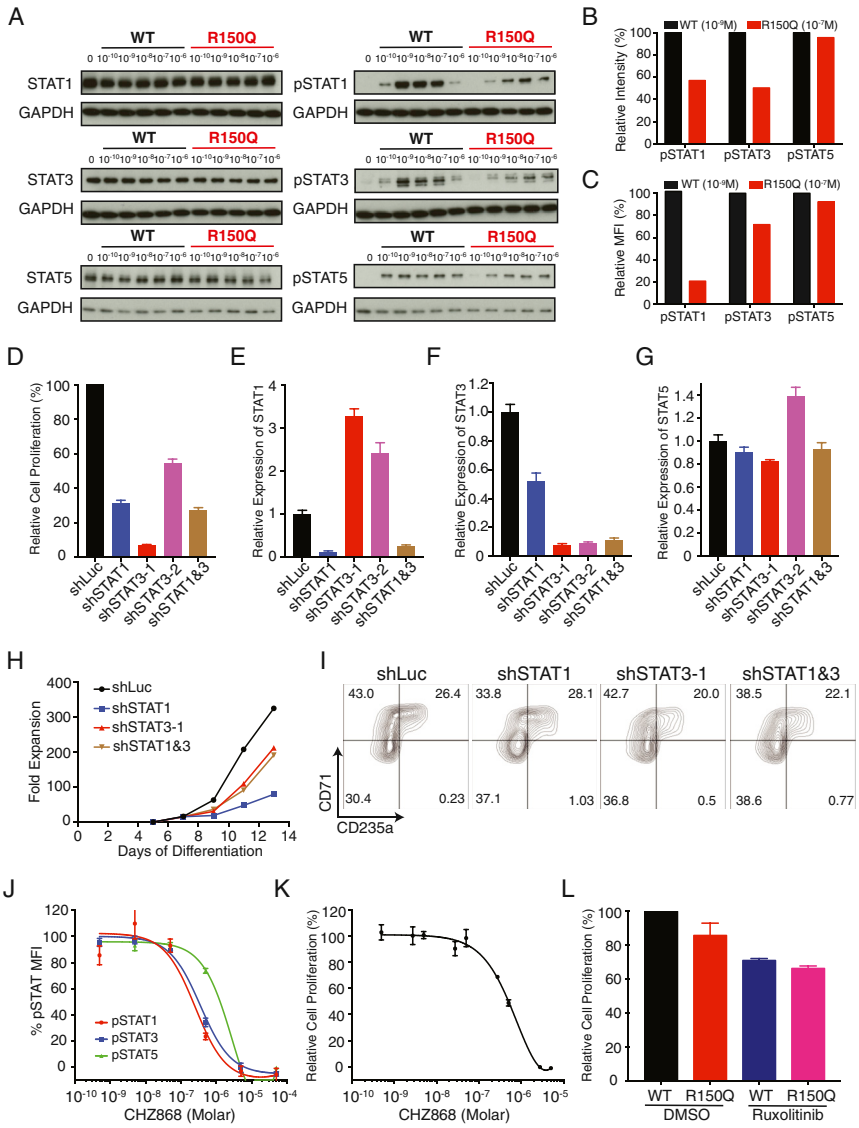

Figure S5. Effect of JAK2 Inhibition on EPO WT or R150Q Mutant Responses, Related to Figure 5

(A) Representative western blots for STAT1, STAT3, STAT5, pSTAT1, pSTAT3, and pSTAT5 after 30 min stimulation with EPO ligands in a dose-dependent manner. GAPDH was used as a loading control.

(B) Relative intensity of pSTAT1, pSTAT3, and pSTAT5 was calculated for EPO WT (10^{-9}M) and R150Q (10^{-7} M). Intensity was normalized to GAPDH.

(C) Relative MFI of pSTAT1, pSTAT3, and pSTAT5 calculated after 1 hr of stimulation with EPO WT (10^{-9} M) or R150Q (10^{-7} M) in CD34-differentiated erythroid cells (day 8). The relative MFI was derived from two experiments.

(D) Proliferation curves of UT7 cells with lentiviral knockdown targeting STAT1, STAT3, or both (STAT1 & 3) with EPO WT (10^{-9} M) after 2 days in culture are shown. Cells infected with shLuc served as a control. Means ± SEM for three independent experiments are shown.

(E) Relative expressions of STAT1 transcripts after lentiviral knockdown targeting shLuc, STAT1, STAT3, or both are shown. Means ± SEM for three experiments are shown.

(F) Relative expressions of STAT3 transcripts after lentiviral knockdown targeting shLuc, STAT1, STAT3, or both are shown. Means ± SEM for three experiments are shown.

(G) Relative expressions of STAT5 transcripts after lentiviral knockdown targeting shLuc, STAT1, STAT3, or both are shown. Means ± SEM for three experiments are shown.

(H) Growth of primary erythroid cells with shRNA-mediated knockdown targeting STAT1, STAT3, or both is shown across the three-phase primary erythroid culture system. Results are shown for a representative culture. Knockdown levels (relative to shLuc control) were 31% for STAT1 alone, 18% for STAT3 alone, and 68 and 38% for STAT1 and STAT3, respectively, with the mixed knockdown.

(I) Erythroid cells on day 7 of differentiation were stained using the surface markers CD235a and CD71 following knockdown targeting STAT1, STAT3, or both. Representative flow cytometry plots are shown.

(J) Percent of pSTAT1/3/5 in UT7 cells following treatment with CHZ868 (JAK2 inhibitor). Mean ± SEM for 3 independent experiments are shown at each concentration. The 100% level of phosphorylation is based on assessment of untreated samples. Sigmoidal fit curves are shown.

(legend continued on next page)

(K) Proliferation curves of UT7 cells of with various concentrations of CHZ868 with EPO WT (10^{-9}M) after 3 days in culture are shown. Means ± SEM for three independent experiments are shown. A sigmoidal fit curve is shown.
(L) Proliferation of UT7 cells with EPO WT (10^{-9}M) and R150Q (10^{-7}M) either with vehicle (DMSO) or Ruxolitinib (40 nM) after 3 days of culture. The results are shown as the mean ± SEM from three independent experiments.

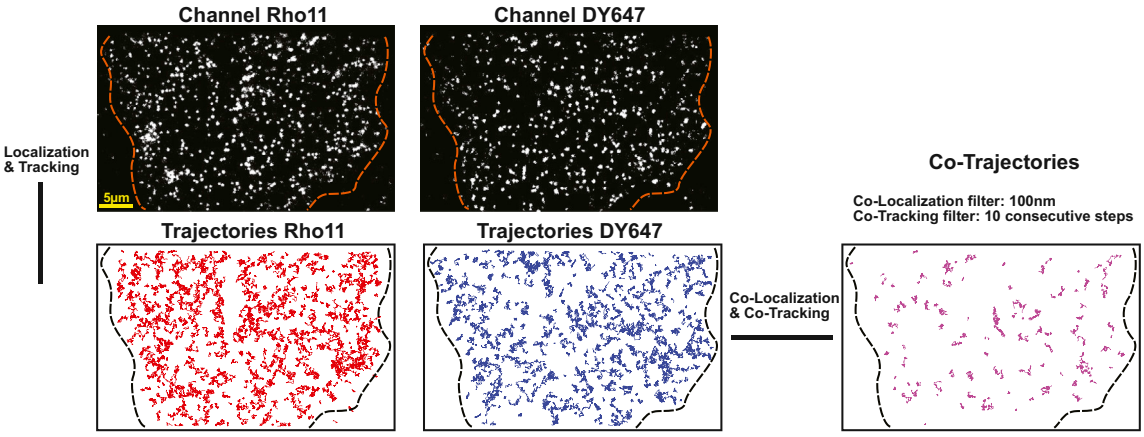

Figure S6. Flowchart of the Co-Localization and Co-Tracking Assay, Related to Figure 6

Particles were considered to be co-localized if found in both spectral channels in the same frame within a distance threshold of 100 nm. The population of co-localized particles was then linked frame-by-frame to co-trajectories (threshold $\geq$ 10 consecutive steps, $\sim$320 ms).